SILICON CARBIDE NANOWIRES AND COMPOSITES

OBTAINED FROM CARBON NANOTUBES

By

YUEJIAN WANG

Bachelor of Engineering, 1996
Tsinghua University
Beijing, P. R. China

Master of Science, 2002
Stephen F. Austin State University
Nacogdoches, TX

Submitted to the Graduate Faculty of the
College of Science and Engineering
Texas Christian University
In partial fulfillment of the requirements
for the degree of

Doctor of Philosophy

December 2006

ACKNOWLEDGEMENTS

I would like to express my sincere thankfulness to my advisor, Dr. T. W. Zerda, for his numerous support, scientific guidance, and continuous encouragement during my research and dissertation completion. I gratefully acknowledge his patience and assistance.

I would like to extend thanks to my teachers, friends, colleagues. I cannot accomplish the requirements of doctoral degree successfully without their kind helps and constructive suggestions. Particularly, I am grateful to Dr. G. A. Voronin, Dr. J. Qian, and Dr. C. Pantea for their assistances in the high-pressure experiments, to Mr. D. Roberts for his training in the electron microscopy operation.

Additionally I would like to thank my parents for their solicitudes and supports, to my wife for her love and understanding throughout my studies. Finally I am grateful to my baby daughter, for she brings lots joyfulness and happiness in my life.

This material is based upon work supported by the National Science Foundation under Grant No. 0502136.

TABLE OF CONTENTS

Acknowledgements……...ii
List of Figures…… v
List of Tables……..…... viii
I. Introduction……..…….. 1
I.1. Diamond and SiC……..…….……..……..6
I.2. Carbon nanotubes and their composites…..……..…….…… 11
II. Experiments……..…….15
II.1. Initial mixtures.…….…… 15
II.2. Apparatus……..…… 15
II.2.1. HPHT equipments…….17
II.2.2. High temperature equipment……...……..20
II.3. Characterization techniques……...……... 21
II.3.1. X-ray diffraction……21
II.3.1.1. Principle of x-ray diffraction (XRD)……. 21
II.3.1.2. Evaluation procedure of x-ray diffraction
profiles by Voigt-function model…….26
II.3.2. Raman spectroscopy……..30
II.3.3. TEM and SEM…….. 33
II.4. Vickers hardness and fracture toughness tests…….. 33
II.5. Basic principle of kinetics of solid state reactions…… 35
III. CNT-silicon reaction under HTHP conditions……...…….…… 38
III.1. CNT-silicon reaction under high temperature……..…... 38
III.1.1. Silicon in the solid state.…….……..…….…….. 38
III.1.2. Silicon in liquid phase……...……...……44
III.1.3. Composition of SiC sintering
in silicon solid and liquid.……49
III.2. Kinetics of CNT-silicon reaction under HTHP…….…….. 54
IV. CNT based diamond composites……. 64
IV.1. CNT/SiC nanocomposites synthesis and characterization.……...…….. 64
IV.1.1. Results……...…….. 64

IV. 1.2. Discussion……..…….67
IV.2. Diamond/CNT/SiC nanocomposites fabrication and characterization… 73
IV.2.1. X-ray diffraction patterns, crystallite size,
and residual strain of the specimens……...…. 73
IV.2.2. SEM images and mechanical properties measurements…….…. 79
IV.2.3. Discussions…….. 82
IV. Summary…….…….86
References……..90
Symbols……...…….. 97
Vita
Abstract

LIST OF FIGURES

1. Fig. 1.1. Illustration of composites.…… 1
2. Fig. 1.2. Crystal structure of diamond.……... 7
3. Fig. 1.3. The tetragonal bonding of a carbon atom with
the four nearest silicon neighbors.……..……. 10
4. Fig. 1.4. Schematic illustration of C60 fullerene.……..…….. 12
5. Fig. 1.5. Schematic illustration of MWNT and SWNT…...……... 13
6. Fig. 1.6. Schematic illustration of graphene sheet rolling up into SWNT…...….. 13
7. Fig. 2.1. Typical TEM image of initial mixture ……...…..……16
8. Fig. 2.2. Piston-Cylinder system, (a) Overview;
(b) High pressure vessel; (c) Sample assembly…….…...……. 18
9. Fig. 2.3. Lindberg furnace……...…….…….……20
10. Fig. 2.4. Geometry of x-ray diffractions.……...…….……22
11. Fig. 2.5. Effect of fine particle size on diffraction curves (schematic).
A — a real experiment; b — an ideal case…….……..……. 23
12. Fig. 2.6. Schematic diagram of x-ray diffractometer……...……... 25
13. Fig. 2.7. A schematic diagram of Raman
scattering effect in a solid ……...……..…… 31
14. Fig. 2.8. Schematic illustration of the shape of Vickers
indenter and the impressed indentation on material…….. 34
15. Fig. 3.1. XRD of samples: (a) initial mixture, (b) mixture
sintered at 1473 K for 1 hour, (c) mixture sintered, and
then oxidized at 1073 K for 1 hour, (d) samples after all treatments
(sintering, oxidation, washing in KOH solution)……..…….40
16. Fig. 3.2. Raman scattering spectrum of sample after all treatments…..…….. 41
17. Fig. 3.3. Typical TEM image of mixture sintered at 1473 K for 1 hour...…..….42
18. Fig. 3.4. Typical TEM image of mixture sintered,
and then oxidized at 1073 K for 1 hour……..……... 43
19. Fig. 3.5. Typical TEM image of sample after all treatments
(sintering, oxidation, washing in KOH solution)…….……..43

20. Fig. 3.6. XRD of samples: (a) initial mixture,
(b) sample S2, (c) sample S3……. 45
21. Fig. 3.7. Raman scattering spectra of samples:
(a) sample S2, (b) sample S3……. 47
22. Fig. 3.8. Typical TEM image of sample S2…..…….…….……48
23. Fig. 3.9. Typical TEM image of sample S3……..……..…….……48
24. Fig. 3.10. Atomic structure of CNTs. The red balls
denote the atoms forming the (7, 5)-(5, 7) rings…….…...… 49
25. Fig. 3.11. X-ray diffraction pattern of sample C_1
obtained at 2 GPa, 1370 K and sintered for 60s.
The insert represents measured (open circles) and
fitted (solid line) diffraction profiles of SiC (220) using
the Voigt function, and the difference between the two
sets of curves is shown in the bottom part of the insert……57
26. Fig. 3.12. Plot of degree of reaction, α, vs. time.
Solid, dash, and dot lines represent the best fit
of the Avrami-Erofeev equation to experimental data for the
(111) reflections at 1270 K, 1320 K, and 1370 K, respectively…… 58
27. Fig. 3.13. Arrhenius plot of the reaction rate constant k
against reciprocal temperature……... 59
28. Fig. 3.14. Plot of domain size of as–grown SiC.
○, ●, and □ represent the experimental data
obtained at 1270 K, 1320 K, and 1370 K, respectively.
Solid, dash, and dot lines represent the best fit of
experimental data obtained at 1270 K, 1320 K,
and 1370 K, respectively…….……...60
29. Fig. 4.1. XRD of the initial Si-CNT mixture (a),
and SiC-CNT samples sintered at T = 1770 K
and 2 GPa (b) and 8 GPa (c). Squares — reflections due
to silicon and CNT; Triangles — reflections due to SiC.…….……..… 65

30. Fig. 4.2. XPS spectra of composites sintered at 1770 K
and 2 GPa, broken line, and 8 GPa, solid line.
Top — C1s region, Bottom — Si2p region..... 68
31. Fig. 4.3. Raman spectrum of the SiC-CNT sample
sintered at 8 GPa and 1770 K, after background
subtraction. 780 nm laser was used as an excitation light…… 69
32. Fig. 4.4. SEM images of ruptured surfaces of
specimens obtained at 1770 K and (a) 2 GPa and (b) 8 GPa.
Agglomerates of silicon carbide coated MWNT
can be recognized in (a)……..… 71
33. Fig. 4.5. X-ray diffraction patterns: (a) initial mixtures;
(b) sample sintered under 5 GPa & 1570 K, C1:
(c) sample sintered under 5 GPa & 2070 K, C4……...……..… 74
34. Fig. 4.6. The (111) peak profiles for the diamond (a)
and SiC (b) phases produced at different temperatures……. 75
35. Fig. 4.7. Measured (Solid line) and fitted (open circles)
diffraction profiles of diamond (111) and SiC (111),
and the difference between the two sets of curves is
shown in the bottom part of the plot…….. 76
36. Fig. 4.8. Plot of microstrain in diamond and SiC vs. temperature……...…… 78
37. Fig. 4.9. SEM images of samples, a) C1, b) C2, c) C3, d) C4.
Arrows indicate the tube-like structures present in the composites…….....81
38. Fig. 4.10. SEM image of a Vickers indentation on composites C1…….……... 83

LIST OF TABLES

1. Table 1.1. The porosity, Knoop hardness (H_K), and fracture toughness of diamond/SiC composites infiltrated at 8 GPa & 2170 K. Uncertainty of the results is indicated by values in parenthesis.…… 4

2. Table 1.2. Parameters of unit cells of 3C-SiC, 2H-SiC, 4H-SiC, 6H-SiC…….9

3. Table 2.1. The values of m for diffusion controlled reactions……...……36

4. Table 3.1. Sintering conditions of samples……55

5. Table 3.2. Kinetics parameters of Avrami-Erofeev model obtained by fitting experimental data to equation 2.25…….……..58

6. Table 3.3. Microstrains inside the as-fabricated SiC…….... 61

7. Table 4.1. SiC phase structural parameters, hardness, and fracture toughness of SiC-CNT composites sintered at 8 GPa and different temperatures…….……..67

8. Table 4.2. Mechanical properties of composites. Uncertainty of the results is indicated by values in the parenthesis…….. 82

I. Introduction

Composites are a combination of at least two chemically distinct materials in which one of the components, called the reinforcing phase, is embedded in the other material named the matrix phase.[1] The reinforcing phase and matrix phase could be metal, ceramic, or polymer. Usually, reinforcing components are strong materials in the form of fibers, sheets, or particles, while the matrix is made of ductile, or tough, materials, as shown in Fig. 1.1. The combination of the strength of reinforcement with the toughness of the matrix under a optimized fabrication process results in composites that may possess unique properties that cannot be achieved by any single component acting alone. We may tailor the overall properties of composites by choosing suitable starting materials and tuning the reaction conditions. There exist lots of composites in our daily life. For example, concrete is a composites made of cement, gravel, and sand, and insert steel skeleton to reinforce it.

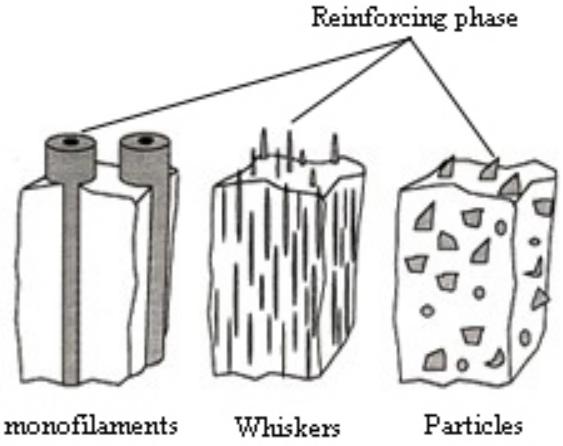

Fig. 1.1. Illustration of composites.[2]

Advanced composite is a broad definition and includes diverse materials, which combine the properties of high strength, high stiffness, low weight, high fracture toughness, corrosion resistance and in some cases, special electrical properties. Among them, diamond composites have attracted a lot of attention, because of their unique mechanical properties and great potential for use in various fields, such as mining, grinding, cutting, drilling.[3-17] Single crystal diamond is the hardest material known to mankind,[18] but its inherent brittleness limits its application in harsh environments of dynamic impacts and high stress concentrations. Many scientists have made concerted efforts toward making diamond composites more flaw-tolerant through the design of their microstructures. In order to manufacture bulk materials containing diamond powder, which starts with single crystal diamond or diamond powder converted directly from graphite, the composites must be fabricated by using a suitable bonding agent under appropriate conditions. It is difficult to directly sinter diamond because some diamond may transform into graphite because of the inhomogeneous distribution of pressure inside the specimen. To avoid this problem, two classes of diamond composites were developed, polycrystalline diamond (PCD) and diamond/SiC composites. For PCD composites, usually cobalt serves as the bonding agent. Under high temperature and high pressure, cobalt melts and infiltrates the voids among the diamond particles. Then cobalt maintains the hydrostatic condition inside the sample and thus prevents the diamond graphitization during sintering process. The next step is to leach out cobalt with a solvent, then the PCD composites mainly consist of diamond crystallites growing together around their contacting area, and the remaining strong C-C bonds retain about

90% modulus of elasticity of diamond.[19] However, even a very small amount of cobalt remaining in the composites after leaching, promotes graphitization of diamond when PCD is exposed to temperature above 1000 K. Graphite impurities reduce the strength and degrade the PCD compacts.

A critical consideration for diamond/SiC composites is to overcome the problem of diamond graphitization by replacing cobalt with SiC as the binding agent. There exist techniques to manufacture diamond/SiC composites, like chemical vapor deposition, vacuum sintering, and high pressure and high temperature (HPHT) sintering. In this dissertation, only the HPHT sintering technique was used to perform the research, and we worked according to the following protocol. Under HPHT, Si melts and fills out cavities among diamond particles, and immediately it starts reacting with diamond. The as-grown SiC serves as a matrix phase to bind all diamond particles together. At the correct ratio of diamond to Si and optimized reaction conditions, all Si will transform into SiC. Strong Si-C bonds explain very high hardness of SiC and make it is possible for diamond/SiC composites to provide excellent mechanical properties.

Extensive research on the diamond/SiC composites synthesis from micron size diamond and silicon powders by HPHT liquid infiltration has been conducted by members of our group.[3-9] Our research showed that mechanical properties of the products highly depend on average grain size of precursors, Table 1.1**.** For example, the hardness remarkably decreases with decreasing crystal sizes of initial diamond. Improvement of fracture toughness is not as pronounced, although a trend is clear — smaller grain sizes of precursors results in better fracture toughness. Besides the grain

size of the precursors, the overall mechanical properties of diamond/SiC composites depend on the concentration of SiC, its structure, density of dislocation, and grain boundaries.

Table 1.1. The porosity, Knoop hardness (H_K), and fracture toughness of diamond/SiC composites infiltrated at 8 GPa and 2170 K. Uncertainty of the results is indicated by values in parenthesis.

Precursors	Porosity	H_K [GPa]	Fracture Toughness [MPa·m$^{0.5}$]
1-2 μm diamond, 44 μm Si	2.9 %	42 (2)	12 (1)
10-14 μm diamond, 44 μm Si	0.6 %	50 (2)	11 (1)
40-60 μm diamond, 44 μm Si	0.3 %	52 (2)	10 (1)

Reduction of grain size below 1 μm leads to unexpected problems. Conventional HPHT infiltration sintering is not suitable when the starting materials consist of submicron or nano size powders due to the so-called self-stop effect.[20] During the sintering process, the newly formed SiC may decrease the open space of tiny pores or block the entrance to a void. This phenomenon is apt to limit or even completely block the infiltration of liquid Si and hence hinder the entire sintering process. To overcome this problem, Qian et al.[4,7] have developed an alternative method, which is based on the simultaneous ball milling of diamond and silicon powder mixtures prior to HPHT sintering. The results showed that after ball milling Si became amorphous and uniformly coated diamonds. The synthesized composites had a unique nanostructure of diamond

embedded into a matrix of nanocrystalline SiC, with large improvement in fracture toughness. These composites showed as much as 50% enhanced fracture toughness while maintaining superhard and superabrasive properties when SiC matrix size decreased from 10 μm to 20 nm. This research revealed the significant effects of nanostructures on mechanical properties of materials. Also, it is in contradiction with the regularly held belief of an inverse correlation between hardness and fracture toughness of materials.

Further reduction of SiC grain sizes by the ball milling technique seems very unlikely. Therefore, we plan to search for another method of producing nanostructure SiC matrix. To accomplish this goal, in this dissertation we will explore possibilities of using carbon nanotube (CNTs) in diamond/SiC composites manufacturing. This novel composite will consist of diamond imbedded into SiC/CNTs matrix obtained by sintering/infiltration technique under high pressure and high temperature. Ideally the CNTs will be distributed along the grain boundary of diamond to form a network structure.

We synthesized this kind of composites by HTHP sintering techniques, under which Si reacted with carbon nanotubes to produce a coaxial structure of carbon nanotubes (inner layers) and SiC (outer layers). Simultaneously liquid silicon reacted with diamond also produced SiC which filled the cavities between diamond crystals. Thus, bonding occurs among diamond, silicon and CNTs. It is assumed that mechanical flexibility of CNTs makes it possible to transfer load from diamond and SiC to CNTs and prevent microcracks from further propagation. The high Young's modulus of carbon

nanotubes together with the reduction of cracks may result in an improvement of fracture toughness of composites.

In current research, x-ray diffraction (XRD) technique played an important role. We used it to evaluate the microstructures of as-made composites and in particular tried to explain their properties by linking them to their unique microstructures. Also, we conducted the kinetics study of SiC formation from Si and CNTs with aid of XRD. The nanocomposites are composed of diamond, Si, and CNTs, so it is necessary to shed light on the reaction mechanism between Si and diamond/CNTs. The reaction between diamond and Si has been already investigated in our research group[21, 22] and in this dissertation we will focus attention on Si reaction with CNTs.

In the following subsections we will describe diamond and SiC, CNTs and their composites. The principles of kinetics study which essentially involved Si and CNTs will be provided in chapter II.

I.1. Diamond and SiC

Diamond is a unique substance, whose properties almost always come out on top, when compared to nearly the rest of materials. As mentioned before, it is the hardest known material, its superior properties embrace many aspects ranging from mechanical (least compressibility, the stiffest) to thermal (the best conductivity with extremely low coefficient of thermal expansion), chemically stable (inert to most chemicals), optical (transparent from ultra-violet to the far infrared), and electronic (negative electron affinity).

All its particular properties could be traced back to its unique atomic arrangement. Diamond is composed of carbon atoms and its space lattice can be viewed as a structure of two interpenetrating face-centered cubic (FCC) lattices displaced along the body diagonal by one quarter of the length of the diagonal. The primitive basis has two identical atoms attached to every lattice point. Thus there are eight atoms occupying the conventional unit cell. The typical bonding characteristic of the diamond is shown in Fig. 1.2. Each carbon atom with four nearest neighbors linked by covalent bonds forms a tetrahedral geometry. These atoms again strongly bond with others. Within single carbon atom, one s-orbital and three p-orbitals undergo sp^3 hybridization. This shared electron-pair bonding forms the strongest known chemical linkage, the covalent bond, and the angle between any two bonds is 109.5^o which results in maximum electronic overlap between neighboring atoms. The nature of C-C bonding is responsible for many

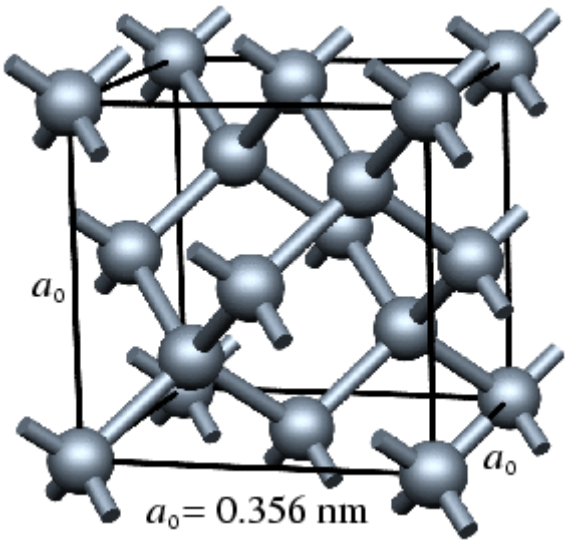

Fig. 1.2. Crystal structure of diamond.[23]

of diamond's superior properties. Breaking the strong bonds requires high amount of heat, hence diamond shows high melting point of near 3500^{o}C. The maximum degree of electronic configuration compact gives a high density (3.52 g/cm^{3}). The electrons are completely shared with neighboring carbon atoms and are not "free" to hop from site to other, which fundamentally gives the explanation to the poor electronic conductivity of diamond. On the contrary, diamond is a good conductor of heat because heat can be dissipated easily by the shared electrons in bonds.

Diamond does not exist in significant quantity in nature, but the market demands on diamond increase day-by-day. This contradiction stimulated efforts to find an effective method to synthesize man-make diamond. Two main methods have been developed during the past fifty years. Both form diamond from carbon. The first approach is the HPHT process and due to its relative low cost it is still widely used.[24-28] Usually this technique produces diamond from graphite under pressure of about 5-10 GPa and temperature ranging from 1700 K to 2500 K, which reproduces the conditions that created natural diamond inside the Earth billions of years ago. The second method uses chemical vapor deposition or CVD; it is basically a method in which a plasma jet, created by the dc arc discharge of CH_4 distilled with H_2, is sprayed onto a Si substrate on which the carbon atoms deposit to form diamond.[29]

Another commonly used material, SiC, has a similar crystal structure to that of diamond with half of carbon atoms in diamond replaced by Si atoms to produce SiC. SiC is one of the most important materials for industrial application and basic research, and has been applied in many areas, from cutting tools to nanoscale electrical devices.

However, unlike diamond, SiC may exist in the form of numerous of polytypes. More than 170 different polytypes have been identified.[30] The most common polytypes are 3C-SiC, 2H-SiC, 4H-SiC, and 6H-SiC, and their parameters are listed in Table 1.2. In

Table 1.2. Parameters of unit cells of 3C-SiC, 2H-SiC, 4H-SiC, 6H-SiC.

	Cell Parameters						System
	a	b	c	α	β	γ	
2H-SiC	**3.081Å**	**3.081Å**	**5.031Å**	**90°**	**90°**	**90°**	**Hexagonal**
3C-SiC	**4.3589Å**	**4.3589Å**	**4.3589Å**	**90°**	**90°**	**90°**	**Cubic**
4H-SiC	**3.081Å**	**3.081Å**	**10.061Å**	**90°**	**90°**	**90°**	**Hexagonal**
6H-SiC	**3.073Å**	**3.073Å**	**15.080Å**	**90°**	**90°**	**90°**	**Hexagonal**

polytype notation system, the first number denotes the periodicity and the following letters C or H refer to cubic and hexagonal structures, respectively. 3C-SiC is referred to β-SiC, and all other polytypes are notated as α-SiC.

Though many polytypes of SiC are in existence, their molecular structure is identical. Except carbon atom covalently bonded with other four Si atom instead of carbon atoms, the entire configuration of unit cell of SiC is similar to diamond, as shown in Fig. 1.3. The distance (marked as "a" in Fig.1.3) between neighboring silicon or carbon atoms is the same, and the distance C-Si is equal to a $(3/8)^{1/2}$ from geometrical considerations. Thus, the distance between two Si layers is a $(2/3)^{1/2}$. The height of unit cell differs from polytype to polytype.

In 1824 Jöns Jacob Berzelius reported the first observation of SiC.[31] However, only after the invention of electric smelting furnace and its application to produce some carbonaceous compounds, the attention started to be attracted onto SiC.[32, 33] Initially SiC

was used as hard material substituting diamond to produce cutting, drilling and polishing tools. Shortly afterwards the interests in electronic properties of SiC came into focus. Today SiC is a fascinating semiconductor that can be operated in harsh environments.[34]

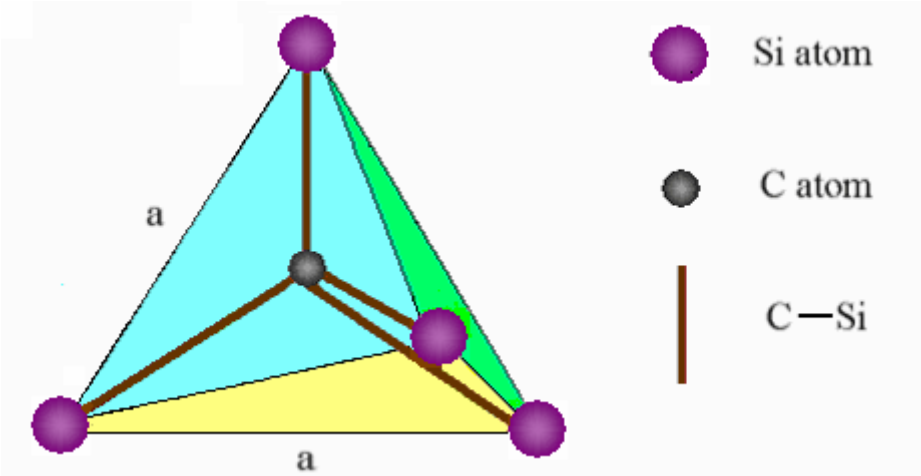

Fig. 1.3. The tetragonal bonding of a carbon atom with the four nearest silicon neighbors.

The physical properties of material critically depend on the size of grains due to the fact that for different grain sizes a significantly different fraction of atoms forms the surface of the grain.[35] When the grain size is reduced to the nanoscale, the corresponding nanostructure shows remarkably different properties from those of microsize or bulk materials. Wong[36] has proved that the strength of the one-dimensional (1D) SiC nanostructure is substantially greater than that of larger SiC structures, and it approaches theoretical values. Consequently, as the reinforcing phase, one-dimensional nanosize SiC is a promising candidate to fabricate superhard nanocrystalline composites.

SiC nanorods were first synthesized successfully in 1995, in the process in which carbon nanotubes were converted to SiC nanorods by reaction with SiO vapor.[37] Subsequently, a number of methods of synthesis of 1D SiC nanostructures have been developed. They fall broadly into the following categories: carbon nanotubes confined reaction;[37, 38] carbothermal reduction of SiO by C nanocapsules or amorphous activated C;[39] chemical-vapor-deposition;[40, 41] reaction between $SiCl_4$ and CCl_4 and metal Na as co-reductant;[42] and annealing carbon nanotubes covered with Si.[43] However, all of the above methods either operated at high temperature via vapour-vapour[39] or solid-vapour[37, 42] reactions, or needed some kind of metal, e.g. Fe, Cu, Ni, as catalyst to cause and speed up the reaction.[40, 41] In this study, to produce SiC nanowires, we used a simple method to directly fabricate 1D SiC nanostructures from mixtures of Si and CNTs at relative low temperature without catalyst. We also revealed how the temperature and pressure affect properties of the final product.

I.2. Carbon nanotubes and their composites

In 1985, C60 fullerenes were discovered by Kroto et al.[44] The 0-dimensional (0D) molecules have a particular shape of a "soccer ball", called "buckyball", as shown in Fig. 1.4. The C60 fullerenes are made up of 60 carbon atoms arranged in pentagonal and hexagonal rings. The discovery and subsequent synthesis of macroscopic quantities of fullerenes has launched a new field in the chemistry and physics of carbon.

Carbon nanotubes were originally discovered as by-products of fullerenes. In 1991 Iijima observed micrometer long multiwall carbon nanotubes (MWNTs), when he

used High-Resolution Transmission Electron Microscopy (HRTEM) to characterize fullerenes grown via the carbon arc method.[46] A model of MWNT is shown in Fig. 1.5.a. Two years later, he and his group discovered single-wall carbon nanotubes (SWNTs),[47]

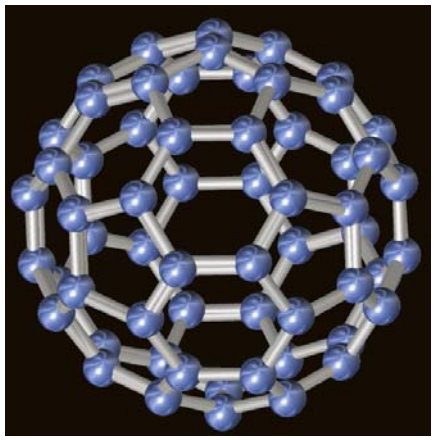

Fig. 1.4. Schematic illustration of C60 Fullerene.[45]

shown in Fig. 1.5.b. Nanotubes belong to the family of fullerenes and can be thought of as elongated buckyballs. An ideal SWNT is a hexagonal network of carbon atoms that is configurationally equivalent to two-dimensional graphene sheet seamlessly wrapped into a cylindrical tube, as demonstrated in Fig. 1.6, while MWNT comprises an array of numbers of coaxial SWNTs. In the ideal case the termination of carbon nanotubes (CNTs) at the ends are fullerene caps or hemispheres.

There is more than one way of rolling up the graphene sheet into CNTs, generating distinct types of CNTs. Three main sort of CNTs are zigzag, armchair, and chiral nanotubes, respectively, which correspond to chiral angles of $\gamma = 0$, 30^{o}, and $0 < \gamma$

$< 30^{o}$. Chiral angle is defined as the angle between the axis of its hexagonal pattern and the axis of the tube.[48]

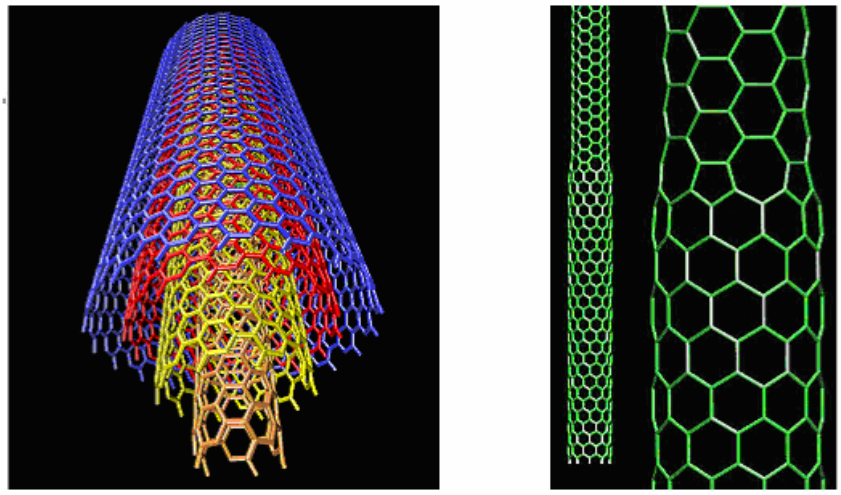

a) b)

Fig. 1.5. Schematic illustration of MWNT and SWNT.[45]

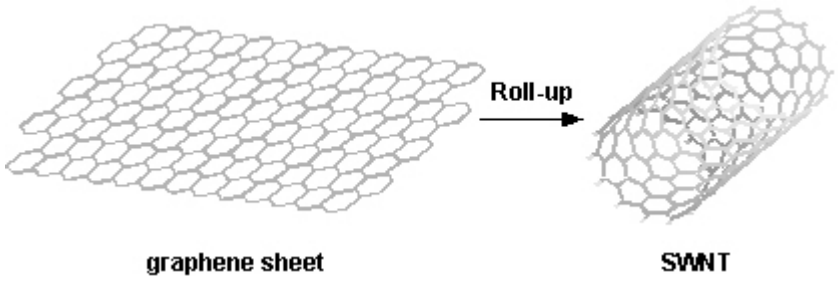

Fig. 1.6. Schematic illustration of graphene sheet rolling up into SWNT.[45]

Since the discovery, CNTs have attracted great interest in the research community because of their specific mechanical and electronic properties. This mainly stems from their one-dimensional (1D) aspect. They are considered to be the building blocks of

future nanoscale electronic and mechanical devices. In this study, we only take advantage of their extraordinary mechanical properties: the Young's modulus as high as 1 Tpa,[49, 50] strength 100 times greater than steel at one sixth of the weight,[45] and high strain to failure.[45] All these properties make CNTs a promising candidate to reinforce some composite materials. The nanotubes reinforcement is been expected to principally improve the fracture toughness of entire composites by absorbing energy during deformation through their highly elastic behavior.

Another result worth noting was published about 10 years ago by Chinese scientists.[51] They fabricated CNTs-nano-SiC composites from a mixture of SiC nanopowders and CNTs by the hot-press method, and claimed that the fracture toughness of the composites was about 10% better than that of a monolithic SiC produced under the same conditions. Besides this article, we have not seen any publication in this particular area.

II. Experiments

II.1. Initial mixtures

In our experiments, the starting materials were multiwall carbon nanotubes, MWNTs, of purity better than 95% and nanosize silicon powders of grain size less than 100 nm and purity higher than 99%, which were both manufactured by Nanostructured and Amorphous Materials Inc., NM. The outer diameter of MWNTs was about 60-100 nm, and their lengths were up to several micrometers. The MWNTs were in the form of loose intertwined tube structures. The method of making uniform mixture of MWNTs and Si was similar to that that has been reported in Ref. 52. MWNTs and Si nanopowders in 3:1 molar ratio were dispersed in absolute alcohol by high-energy sonication using an ultrasonic processor (Sonic and Materials, Inc.) at 60 W. The dispersing time was approximately 30 minutes. Then the mixture solution was poured into a culture dish to evaporate the alcohol. In order to prevent the MWNTs and Si particles from separating in solution, the dish holding solution was placed into a running ultrasonic cleaner. When it was dry, the mixture of MWNTs and Si nanopowders was uniform as verified by TEM analysis. Typical TEM images (Fig. 2.1) of the initial mixture showed twisted and interweaved carbon nanotubes with a significant fraction of nanosize silicon particles attached to carbon nanotubes.

II.2. Apparatus

Usually HPHT equipments are used in physics, geology, and material science to investigate micro-behavior of materials under various HPHT conditions. In our case,

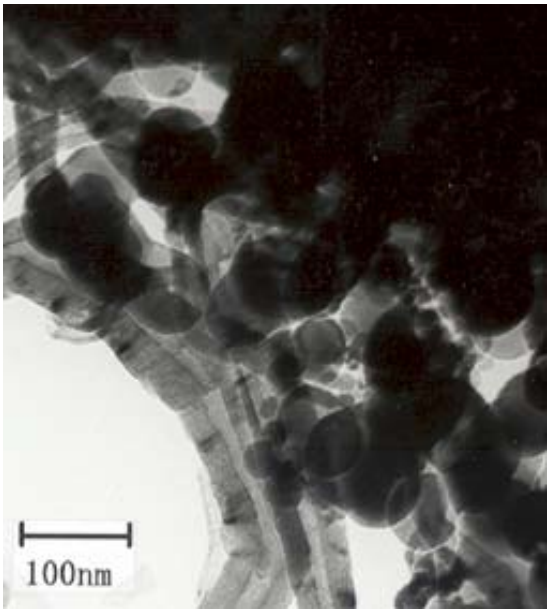

(a)

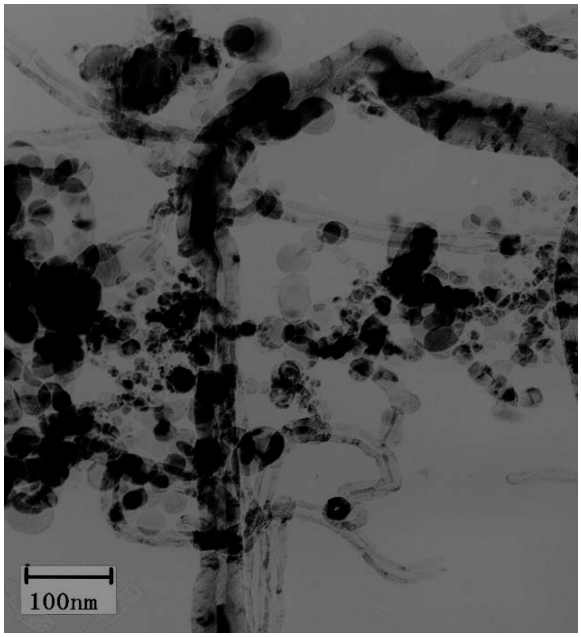

(b)

Fig. 2.1. Typical TEM image of initial mixture.

since high pressure can lower the Si melting temperature, control the C-Si reaction rate, compress the materials, and reduce the SiC grain overgrowth, we employed HPHT equipment to investigate the kinetics of solid state reaction between MWNTs and Si and to produce MWNTs based composites. Additionally, the conventional furnace was involved in our research to synthesize SiC nanowires.

II.2.1. HPHT equipment

Although several different press designs exist, the principle for high-pressure achievement remains the same. First, pumping systems load a large force on upper and lower rams through pressure medium (air or hydraulic fluid). Then high pressure is obtained via a dramatic decrease of working area from the ram to the sample within the pressure cell.

The high pressure origins from a four-post solid steel press, which consists of an associated hydraulic pumping package, stack components, a pressure vessel.[53] The capacity of the system is 250 tons. Dr. Qian[9] and Dr. Pantea[54] have already given detailed information about that press, here I will provide a brief description of the high pressure cell.

a) Piston-cylinder system

As its title clearly indicates, the key component of the piston-cylinder system mainly consists of two parts: piston and cylinder, as demonstrated in Fig. 2.2. Both are made of one of the strongest materials, tungsten carbide (WC). Moreover, the radial pressure existing between the WC core and stainless rings reinforces the cylinder.

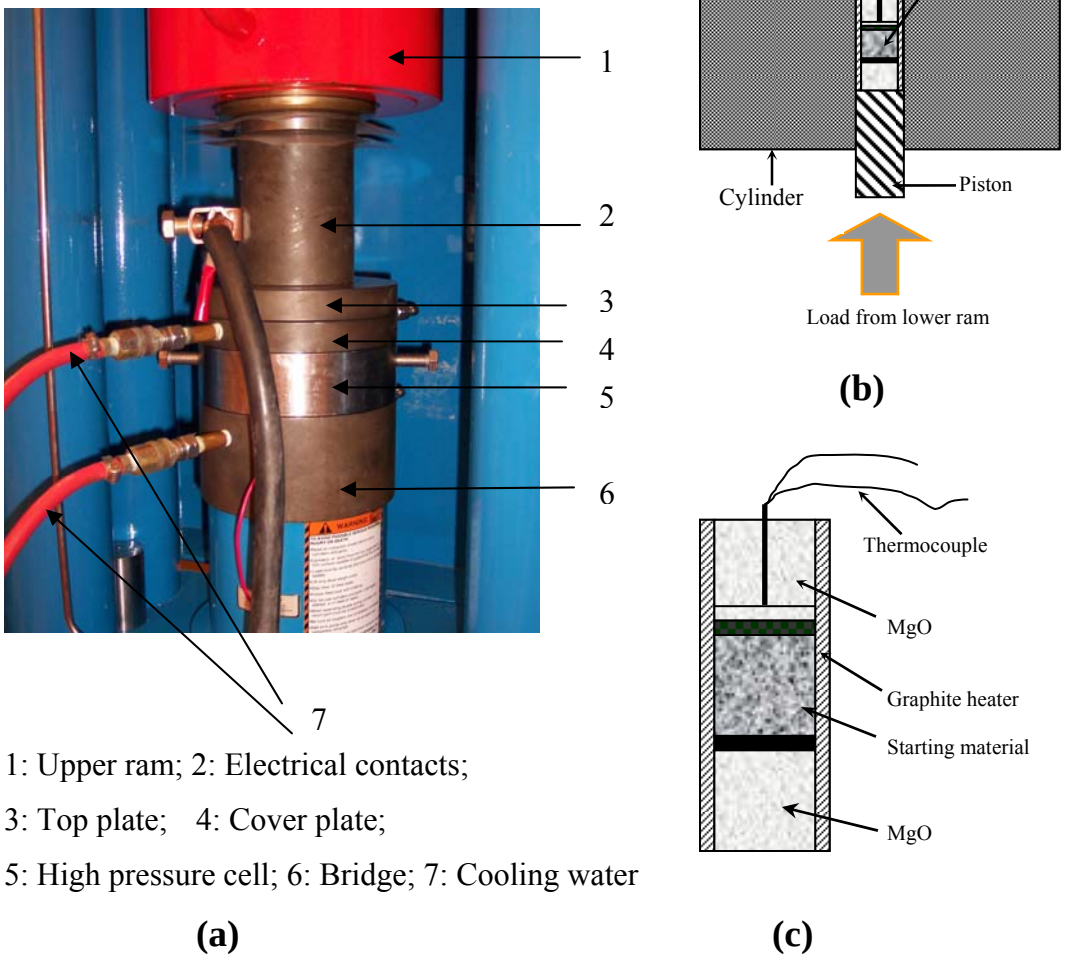

Fig. 2.2. Piston-Cylinder system; (a) Overview; (b) High pressure vessel; (c) Sample assembly.

The high pressure is realized using two separate hydraulic rams. A loading force supplied by upper ram compresses the pressure vessel against the top plate of the press to prevent lateral fracture of the cylinder perpendicular to its axis. The load transmitted from the lower ram pushes the piston upward and squeezes the sample

located in the cylindrical hole of the cylinder to achieve the desired pressure. This system can reach hydrostatic pressure of up to 3.5 GPa. The pressure readings are accurate to within ±2%.

The high temperature is achieved by electrical current passing through a cylindrical graphite heater within which the sample is located. The temperature inside the sample is measured by a D type thermocouple, and can be directly read on display board. By controlling the amount of the electrical power output, we can easily obtain the desired temperature. The highest temperature achieved safely is around 2400 K. Temperature is stable within ±1% of the terminal temperature.

b) Toroidal anvil cell

Toroidal anvil cell was first developed by scientists of the Soviet Union to produce hydrostatic pressures greater than 5.0 GPa at high temperature in a large working volume. It consists of two identical tungsten carbide anvils with toroidal grooves and an associated lithographic stone gasket that matches the contours of the grooves.[17] This particular structure of toroidal anvil cell effectively avoids the deformation of the flat face anvil under high pressure. The sample is placed in the central cylindrical hole of gasket located between two anvils. When the anvils move toward each other under the loading force pushing, the gasket suffers compression, which results in high-pressure generation inside.

Unlike piston-cylinder system, we cannot read the temperature directly and we must use the calibration curve to determine the temperature and pressure inside the sample. The calibration curve was reliable and the estimated deviations stay within ±50

K for temperature and ±0.5 GPa for pressure. For the detailed calibration procedure, see the above-mentioned dissertations.

c) Experiment running protocol

The experiments were run according to the following protocol. The pressure was raised to the terminal value at room temperature. Next, the desired temperature was reached at a rate of 200 K/sec, and the samples were kept at that temperature for various time. Finally, temperature was decreased to the room level and the pressure released.

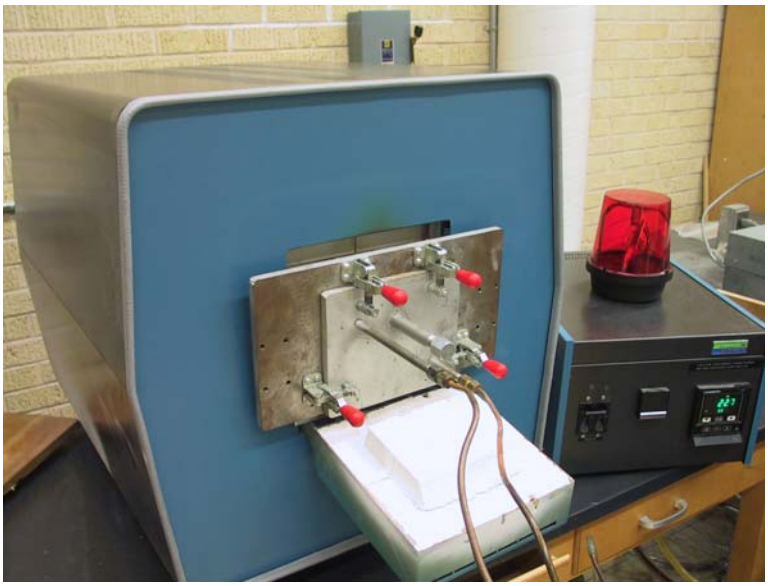

Fig. 2.3. Lindberg furnace.

II.2.2. High temperature equipment

A box furnace, Fig. 2.3, made by Lindberg/Blue M Company, was used in our experiments to produce SiC nanowires. The Furnace is constructed with rugged firebrick

insulation for stability, silicon carbide heating elements to maximize heat transfer, insulating door plug and swing-down door. The highest temperature achieved by furnace is 1773 K. When pure argon or nitrogen flowing through to purge the furnace, the highest temperature reached was around 1523 K.

II.3. Characterization techniques

In our research x-ray powder diffraction (XRD) was used to identify the materials, to compute the domain sizes and microstrains inside the sample, and to estimate the activation energy for SiC formation from Si and CNTs. Raman spectra were applied to conform the composition of samples. The shapes and morphologies of specimens were recorded by using canning electronic microscopy (SEM) and Transmission electron microscopy (TEM).

II.3.1. X-ray diffraction

II.3.1.1. Principle of x-ray diffraction

XRD is one of the most important, powerful and widely used techniques which are applicable to a broad investigation of physical, chemical, mechanical properties of materials.[55] The XRD technique is based principally on the Bragg's law, which first explained the x-ray diffraction effects in term of "reflection" from a stack of parallel atomic planes.[56] Fig. 2.4 shows a section of a crystal, its atoms arranged on a set of parallel planes A, B, C, D, … normal to the plane of the drawing and a distance d apart

between planes. When a beam of perfectly parallel, monochromatic x-rays with wavelength λ strikes a crystal face at an angle θ_B, called the Bragg angle, some portion of

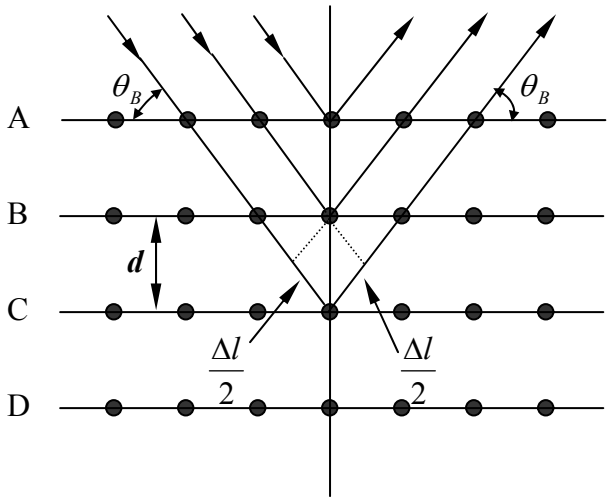

Fig. 2.4. Geometry of x-ray diffractions.

the incident beam will penetrate several million atomic layers, and at each atomic plane a minute part of the beam is reflected. These x-rays reflected from successive planes will create a constructive interference when the path difference Δl is equal to a whole number n of the x-ray wavelength:

$$\Delta l = 2d \sin\theta_B = n\lambda \qquad (2.1)$$

When incident x-rays propagate along angles only slightly different from θ_B, it is observed that destructive interference is not complete. Let us consider two limiting angles, $2\theta_1$ and $2\theta_2$, at which the diffracted intensity must drop to zero. It follows that the diffracted intensity at angles near $2\theta_B$, but not greater than $2\theta_1$ or less than $2\theta_2$, is not zero but has a value intermediate between zero and the maximum intensity of the beam

diffracted at an angle $2\theta_B$. The curve of diffracted intensity vs. 2θ will thus have the form of Fig.2.5.a in contrast to Fig. 2.5.b, which illustrates the hypothetical case of diffraction occurring only at the exact Bragg angle.

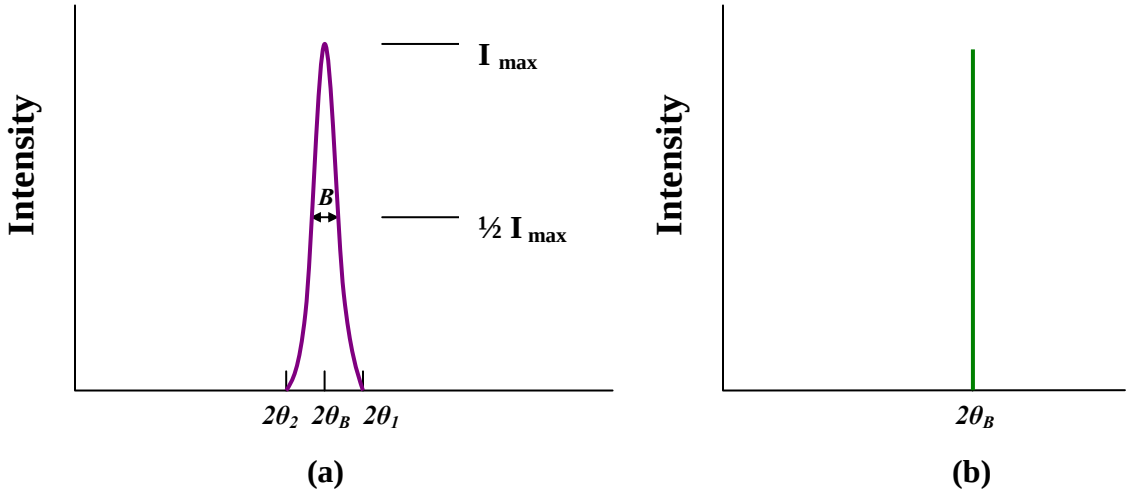

Fig. 2.5. Effect of fine particle size on diffraction curves (schematic).

A — a real experiment b — an ideal case

The width B of the diffraction curve of Fig. 2.5.a is related to the thickness of the crystal t. It has been proved that B increases as t decreases. The width B is measured, in radians, at an intensity equal to half of the maximum intensity. As a rough measure of B, we can take half the difference between the two extreme angles at which the diffracted intensity is zero, assuming the diffraction line is triangular in shape. Therefore,

$$B = \frac{1}{2}(2\theta_1 - 2\theta_2) = \theta_1 - \theta_2 \qquad (2.2)$$

We now write the Bragg law equations for these two angles, which are related to the thickness of crystal rather than to the distance between adjacent planes:

$$2t\sin\theta_1 = (m+1)\lambda \tag{2.3}$$

$$2t\sin\theta_2 = (m-1)\lambda \tag{2.4}$$

By subtraction we find

$$t(\sin\theta_1 - \sin\theta_2) = \lambda \tag{2.5}$$

$$2t\cos(\frac{\theta_1+\theta_2}{2})\sin(\frac{\theta_1-\theta_2}{2}) = \lambda \tag{2.6}$$

But θ_1 and θ_2 are both very nearly equal to θ_B, so that

$$\theta_1 + \theta_2 \approx 2\theta_B \tag{2.7}$$

and

$$\sin(\frac{\theta_1-\theta_2}{2}) \approx (\frac{\theta_1-\theta_2}{2}) \tag{2.8}$$

Therefore

$$2t(\frac{\theta_1-\theta_2}{2})\cos\theta_B = \lambda \tag{2.9}$$

$$t = \frac{\lambda}{B\cos\theta_B} \tag{2.10}$$

A more accurate treatment of the problem gives

$$t = \frac{0.89\lambda}{B\cos\theta_B} \tag{2.11}$$

which is known as the Scherrer equation with constant K = 0.89. It is used to estimate the particle size of very small crystals from the measured width of the individual x-ray diffraction peak. However, Scherrer formula is limited to situation in which only small

size effect contributes to the width *B* of the pure diffraction profile, since other effects from microstrains or instruments also may lead to peak broadening.

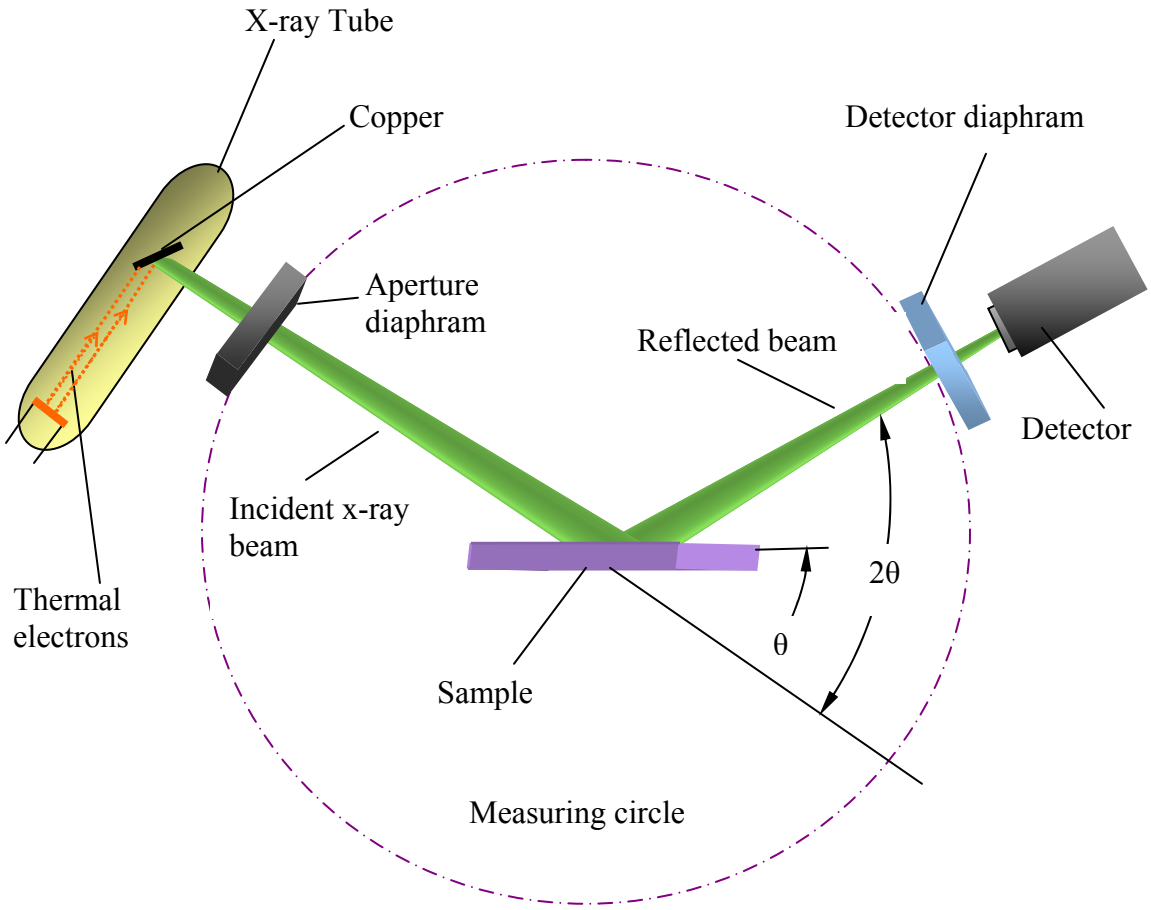

Fig. 2.6. Schematic diagram of x-ray diffractometer.

θ: Glancing angle; 2θ: Diffraction angle

X-ray diffraction patterns were obtained on a Philips PW2773 diffractometer. Fig 2.6 is a schematic diagram of a powder x-ray diffractometer. The x-ray radiation is emitted by copper, whose characteristic wavelength for the Kα radiation is equal to

1.54056 Å. When the incident beam strikes a powder sample, diffraction occurs in every possible orientation of 2θ. The diffracted beam is detected by using a moveable detector, which is connected to computer which controls the running of x-ray diffractometer and records x-ray patterns. During the measurements, diffractometer was operated at 35 kV and 30 mA; 2θ ranged from 20^o to 110^o with a step of 0.02^o and an exposure time of 3 seconds.

Because the peak broadenings of our samples were caused by the combination of the small size effect (such as nano-particles) and the elastic strains introduced by dislocations, Scherrer formula cannot accurately interpret the corresponding microstructures. Hence, after we obtained XRD patterns, the more complicated techniques, integral breadth method was applied to identify the size and strain factors. In the following section, we will give a detailed description of this analytic technique.

II.3.1.2. Evaluation procedure of x-ray diffraction profiles by Voigt-function model

Analysis of x-ray band profile began when Scherrer observed that small crystallites caused broadening of diffraction lines, and derived a formula that relates the line broadening to crystallites size, as described in the past section Eq. 2.11.[57] Stokes and Wilson observed that strained or imperfect crystals cause line broadening of a different sort, than the broadening that arises from small crystallite size. They formulated a complex and exact theory of line broadening. Soon afterwards, Stokes adapted the Fourier-deconvolution method to extract the pure physical line profiles from the observed

pattern. A more comprehensive line-broadening theory[58, 59] attributes the diffraction line broadening to two main kinds of physical effects: size and strain components. This theory has been widely applied to metals, alloys, oxides, and polymers. Further development is due to Rietveld[60] who adopted a full pattern fitting procedures. After Lanford (1978) introduced a Voigt function in the field of x-ray powder diffraction and adopted it in the Rietveld analysis, the integral-breadth fitting methods become more practical.

Besides the crystallite size and microstrains, instruments also could give rise to the line broadening of patterns.

$$h(x) = g(x) * f(x) + \text{background} \tag{2.12}$$

$$g(x) * f(x) = \int g(z)f(x-z)dz \tag{2.13}$$

The observed, physical, and instrumental profiles are named as $h(x)$, $f(x)$, and $g(x)$, respectively. In order to obtain the correct microstructure parameters of specimen, a correction to observed line profile h for instrumental effects has to be performed. In the present research, a standard bulk silicon supplied with x-ray instrument, showing minimal physical broadening, defined the instrumental contribution to the observed line broadening.

The choice of method to remove or minimize the instrument broadening contribution is of utmost importance for the further line-broadening analysis. Usually, we employ the convolution-fitting method to extract the pure physically broadened line profiles from the observed profiles. In this approach, the simulated line profile is built according to Eq. 2.12 and adjusted by a least-square fitting. Moreover, it requires $f(x)$

and *g(x)* to be modeled by suitable analytical functions whose breadths can be separated. Among the several used functions, e.g. Gauss, Cauchy, and their sums, the Voigt function shows the best fitting of the actually x-ray peak profiles, and long-term experiences proved that the Viogt function is a satisfactory approximation for most purposes, which model the physically broadened (size-strain line broadening) diffraction profiles as a convolution of Gauss and Cauchy functions. The corresponding Gauss and Cauchy integral breadths, defined as the width of a rectangle having the same area A and height as the observed line profile[55], can be derived for *g(x)* and *h(x)*, and hence *h(x)*. The procedure has been described by Langford in 1992.[55]

Once the physical broadening profile is obtained, it is possible to separate the size and strain broadenings and to consider their origins. The size and distortion integral breadths of Cauchy (β_{SC} and β_{DC}) and Gauss (β_{SG} and β_{DG}) components comply with the convolution principle, and the relations have been derived:

$$\beta_C = \beta_{SC} + \beta_{DC} \frac{s^2}{s_0^2} \tag{2.14}$$

$$\beta_G^{\,2} = \beta_{SG}^{\,2} + \beta_{DG}^{\,2} \frac{s^2}{s_0^2} \tag{2.15}$$

β_{SC}, β_{DC}, β_{SG}, and β_{DG} could be obtained from at least two reflections. Surface- and volume-weighted domain sizes are directly expressed by equations:

$$< D >_s = \frac{1}{2\beta_{SC}} \tag{2.16}$$

$$< D >_v = \frac{\exp(k^2)}{\beta_{SG}} \mathrm{erfc}(k) \tag{2.17}$$

where $k = \beta_{SC}/(\pi^{1/2}\beta_{SG})$ is the characteristic integral-breadth ratio of a Voigt function and erfc(k) is the error function complement. In addition, this method allows characterization of microstrains in crystals. Microstrains can be evaluated from the average distance L perpendicular to the diffracting planes and parameters β_{DC} and β_{DG}:

$$< \varepsilon^2(L) > = \frac{1}{s_0^2}\left(\frac{\beta_{DG}^2}{2\pi} + \frac{\beta_{DC}}{\pi^2}\frac{1}{L} \right). \tag{2.18}$$

Here it may be worth clarifying the terms of domain size and strain. All the possible effects that could result in size broadening, e.g. stacking or twin faults, small-angle boundaries caused by dislocation ordering, grains, or similar extended lattice defects, are put in the common category "coherent domain size" distinctly defined by coherent diffraction. In most cases, we cannot limit the x-ray domain size to particle or grain size, obtained through other techniques. The definition of strain embraces all contributions from any distortion of a regular lattice, such as dislocations and various point defects. These two effects are interconnected, which is one of the reasons why it is not easy to interpret the underlying physics of broadened line profiles.

In this dissertation, all the domain sizes and microstrains were calculated by two programs: BREADTH[61, 62] and SHADOW[63-65]. SHADOW is a profile fitting program which corrects the influence of instrument with the aid of the calibration file, determines the background, performs the peak finding, and refines the parameters describing the

diffraction profiles. The program BREADTH computes the microstrain, both area- and volume-weighted domain sizes, together with the corresponding estimated standard deviations.

II.3.2. Raman spectroscopy

Raman spectroscopy is a powerful, sensitive, non-destructive technique for material identification and product quality investigation.[66] Raman effect in solids is an inelastic scattering of the incident photons by the crystal electrons distributed around the lattice nuclei. In the photon-electron interaction, the incident photons exchange a quantum of energy with the electrons via the creation or annihilation of the lattice vibrations (phonons). As a result, the scattered photons lose or gain an energy quantum depending on whether a photon was created (Strokes process) or annihilated (anti-Strokes process).[67] In Raman spectroscopy, the energy of the scattered photons is measured; thus, a characteristic value of the vibration energy of a specific material may be obtained.

The origin of Raman spectra is briefly illustrated on Fig. 2.7. The sample is irradiated by a monochromatic laser beam of frequency ν_o. The scattered light consists of two types: one that arises from the elastic Rayleigh scattering, called Rayleigh scattering, which is strong and has the same frequency as the incident beam (ν_o); and the other called Raman scattering, which is very weak and has frequency $\nu_o \pm \nu_m$, where ν_m is a vibrational frequency of crystal molecule. The $\nu_o+\nu_m$ and $\nu_o-\nu_m$ lines are named the Stokes and anti-Stokes lines, respectively. Thus, in Raman spectroscopy, we measure the vibrational frequency (ν_m) as a shift from the incident beam frequency ν_o.[68]

A classic description of the Raman scattering has been developed by Placek.[69] We give a very simple classical model to show how the Raman effect arises. It starts from the relation

$$P = \alpha E \tag{2.19}$$

between the electric field amplitude $E = E_0 \cos(2\pi v_0 t)$ of the incident laser and the electric dipole momentum *P*. We assume that a diatomic molecule is irradiated by the laser. Here, α, a proportionality constant, is called polarizability. The nuclear displacement q is written

$$q = q_0 \cos 2\pi v_m t \tag{2.20}$$

where q_0 and v_m are the vibrational amplitude and frequency of molecule, respectively. For a small polarizability, we can expand it into Taylor series in the nuclear

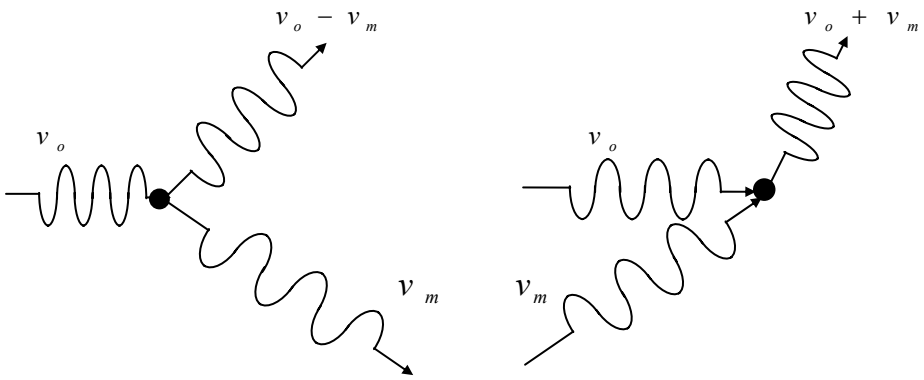

Stokes Raman (phonon creation) Anti-Stokes Raman (phonon annihilation)

Fig. 2.7. A schematic diagram of Raman scattering effect in a solid.

displacements

$$\alpha = \alpha_0 + \left(\frac{\partial \alpha}{\partial q}\right)_0 q_0 + \cdots \tag{2.21}$$

Here, α_0 is the polarizability at the equilibrium position, and $(\partial\alpha/\partial q)_0$ is the rate of change of α with respect to the change in q, evaluated at the equilibrium position. Substituting (2.20) and (2.21) into (2.19), we obtain

$$\begin{aligned} P &= \alpha E_0 \cos(2\pi v_0 t) \\ &= \alpha_0 E_0 \cos(2\pi v_0 t) + (\partial\alpha/\partial q)_0 q E_0 \cos(2\pi v_0 t) \\ &= \alpha_0 E_0 \cos(2\pi v_0 t) + (\partial\alpha/\partial q)_0 q_0 E_0 \cos(2\pi v_0 t)\cos(2\pi v_m t) \\ &= \alpha_0 E_0 \cos(2\pi v_0 t) + \frac{1}{2}(\partial\alpha/\partial q)_0 q_0 E_0 \{\cos[2\pi(v_0 + v_m)t] + \cos[2\pi(v_0 - v_m)t]\} \end{aligned} \tag{2.22}$$

According to the classical theory, these three terms correspond to the Rayleigh scattering and Raman scattering of frequency $v_0 + v_m$ (anti-Stokes) and $v_0 - v_m$ (Stokes), respectively. Thus, we see how the Stokes and anti-Stokes scattered lines arise from phonons modulating the electronic polarizability. The scattered light intensity is proportional to $P^2(t)$ and hence to E^2.

Raman spectroscopy is a particularly useful tool to characterize carbon-related materials, because, for different carbon phases, diamond, graphite, and carbon nanotubes, their characteristic vibration peaks exist in different regions. Raman scattering spectra were obtained at room temperature using a homemade Raman microimaging system which consists of a laser, a microscope, a spectrometer and a CCD detector. The 514 nm line of an Ar^+ laser was used as the excitation line. The spectral resolution was 4 cm^{-1}.

II.3.3. TEM and SEM

The morphology and microstructure of starting materials and final products were investigated using Philips-EM 300 TEM operated at 60 KV and JSM-6100 SEM operated at 20 KV. For TEM study, a small amount of sample was dispersed into ethyl alcohol by ultrasonic cleaner for 20 minutes, then a couple of drops of the mixed solution were placed onto a carbon coated 200 mesh copper grid. As the alcohol solvent was evaporated, a film of sample was mounted on the grid.

II.4. Vickers hardness and fracture toughness tests

Because of the extreme hard surface of ceramic composites we made, Vickers hardness was selected as the measure of hardness of the specimens. The Vickers indenter is a square-based pyramid whose opposite sides meet at the apex at an angle of 136^{o}. During a measurement, the diamond indenter is pressed into the surface of the material at loads F. After unloading, the size of impression is measured under microscope or SEM. The schematic illustration of indenter impression is shown in Fig. 2.8. The Vickers number (HV) is proportional to the loading force F (measured in kilograms-force), but inverse to the area of the indentation:

$$HV = 1.854(F/d^2) \qquad (2.23)$$

with d the average length of diagonal line of the indentation.

The diamond indenter has advantages over other indenters, because it is not deformed over time and use, and also the dark square impression left by the indenter penetration is more easily read for area size under light background.

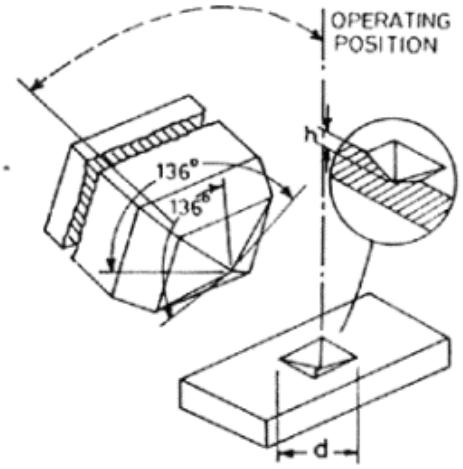

Fig. 2.8. Schematic illustration of the shape of Vickers indenter and the impressed indentation on material.[9]

The Vickers hardness measurements were carried out through using a Buehler Micromet 2003 tester with a load of 4.9 N; and we measured the size of indentation with the aid of SEM. The fracture toughness stress intensity factor K_{IC} was measured on a Buehler Macromet tester by using a Vickers diamond indenter with a load 147 N. After indentation we immediately took the post-indentation images. Then, the lengths of the cracks C, if any, that do emanate from the corners of the Vickers indentation, were measured directly from the *in-situ* images. The fracture toughness was calculated using the following analytical expression:

$$K_{IC} = 0.026E^{1/2}F^{1/2}d/C^{3/2} \qquad (2.24)$$

Where E, F, D, and C refer to elastic modulus, loading force, average length of diagonal line of the indentation, and the lengths of the cracks at the corner of indentation, respectively.

II.5. Basic principle of kinetics of solid state reactions

In a reaction system, not all the particles undergo the transformation at the same time and at any time only a fraction of particles is available to participate in the transformation. The coexistence of reactants and products throughout the transformation is due to the simple reason that only a fraction of particles have free energy higher than E_a, activation energy, therefore, energetically suitable for the transformation.[70] During the transformation, an atom or group of atoms continuously receives energy until its thermal (kinetic) energy reaches the activation energy level, subsequently undergoes transformation and then its free energy decreases to the final value. The activation energy is an energetic threshold for the transformation occurrence.

There are several approaches to describe a solid-state reaction. The most common model for the nucleation and growth process has been developed by Avrami[71] and Erofeev[72]. It states that nucleation starts at nucleation sites that already exist randomly dispersed in the precursor phase and then the density of germ nuclei diminishes because some of them become growth nuclei for grains of new phase and grains grow by ingestion other nuclei[71], and most part of the growth of products is sustained by reactants diffusion across the as-grown product layers.[70] The Avrami-Erofeev equation is represented by:

$$\alpha(t) = 1 - \exp[-(kt)^m] \tag{2.25}$$

where k, the reaction rate constant, is the rate at which a reaction proceeds and could be expressed either in term of the rate of generation of any of the products or that of consumption of any of the reactants,[70] while m is a parameter that relates to reaction mechanism, nucleation rate, and geometry of the nuclei, and its possible values are listed on Table 2.1.[54]

Table 2.1. The values of m for diffusion controlled reactions.

	Growth type	m
Constant nucleation rate	3-dimensional (spheres)	2.5
	2-dimensional (plates)	2.0
	1-dimensional (rods)	1.5
Zero nucleation rate (saturation of point)	3-dimensional (spheres)	1.5
	2-dimensional (plates)	1.0
	1-dimensional (rods)	0.5
Decreasing nucleation rate	3-dimensional (spheres)	1.5-2.5
	2-dimensional (plates)	1.0-2.0
	1-dimensional (rods)	0.5-1.5

α(t), a dimensionless parameter in equation (2.25), called the degree of reaction, is used to express the kinetics equation of reaction. In our study, the degree of reaction is defined as:

$$\alpha = \frac{m_{Si}^{reacted}}{m_{Si}^{initial}} = \frac{m_{Si}^{reacted}}{m_{Si}^{reacted} + m_{Si}^{remaining}} \tag{2.26}$$

Due to the mass relationship between Si and SiC, we rearranged the above equation as following:[54]

$$\alpha = \frac{0.70045 \times m_{SiC}^{as-grown}}{0.70045 \times m_{SiC}^{as-grown} + m_{Si}^{remaining}} \tag{2.27}$$

The time dependent sintering parameter α (t) for various specimens was calculated from the intensity ratio of the diffraction peaks due to Si and SiC. This parameter reveals the change of the mass fraction of product.

III. CNT-silicon reaction under HTHP conditions

III.1. CNT-silicon reaction at high temperature

This section presents a discussion on 1D SiC nanostructures fabricated at different *P-T* conditions. The motivation of this project is to explore the mechanism of the reaction between CNT and silicon in the solid and liquid phases, and to reveal the relationships between properties of the final products and reaction conditions. Three experiments were carried out: one at 1473 K and ambient pressure, second one at 1723 K and ambient pressure, and third one at 1723 K and 0.5 GPa.

III.1.1. Silicon in the solid state

a) Sample preparation: The mixture of MWNTs and Si nanopowders in 3:1 molar ratio was compressed at room temperature by applying low pressure of about 20 MPa (200 bars), for several minutes, into solid tablets. These tablets were placed in a Vycor crucible, which was then placed into a conventional furnace. It took 8 hours to raise temperature to 1473 K, almost 200 degrees below silicon melting point at ambient pressure. The mixtures were sintered at that temperature for about one hour and then furnace was allowed to cool down to room temperature overnight. During the whole operation the furnace was purged with pure argon.

b) Sample cleaning procedure: the as-fabricated samples were oxidized at 1073 K for 1 hour to remove the remaining MWNTs and other forms of carbon. After the oxidization procedure, the samples were treated with hot dilute KOH (20 wt.%) to etch

Si, and finally washed using absolute alcohol and distilled water. The purified sample was named as S1.

III.1.1.1. X-ray diffraction patterns

Fig. 3.1a shows XRD pattern of the initial mixture of MWNTs and Si nanopowders. The XRD spectrum indicates that the mixture was composed of MWNTs and Si. The diffraction peaks of Si are narrower and more intense than those of MWNTs. Because of low content of MWNTs in the mixture, only two peaks, (002) and (100), can be observed clearly. Fig. 3.1b shows XRD pattern of the mixture after sintering at 1473 K for 1 hour. Compared to Fig. 3.1a, a new series of peaks appeared, and the peaks due to MWNTs and Si did not change significantly. It confirms that new material has been synthesized, but the reaction was incomplete, and most of MWNTs and Si remained unreacted. The new diffraction peaks can be indexed to the known β-SiC with lattice constant a = 4.348Å, which is consistent with the value given in the literature as a = 4.359 Å. Fig. 3.1c shows XRD pattern of the sample sintered and then oxidized at 1073 K for 1 hour. There are no diffraction peaks of MWNTs at all indicating that the remnants of MWNTs have been removed successfully. The specimen contained only Si and β-SiC. It implied that the as-synthesized β-SiC phase and the MWNTs phase were separated. If β-SiC had coated the MWNTs, the inner MWNTs would have been isolated by β-SiC layers from the flowing fresh air and would survive during the oxidization process. After oxidation and treatment in KOH in x-ray diffractograms Fig. 3.1d, we observed only peaks due to SiC. β-SiC diffraction peaks are obviously broad and

asymmetric, which may be attributed to the reduction in crystallite sizes and increased population of stacking faults in β-SiC. Meanwhile, the XRD patterns proved that our sample cleaning approach worked efficiently.

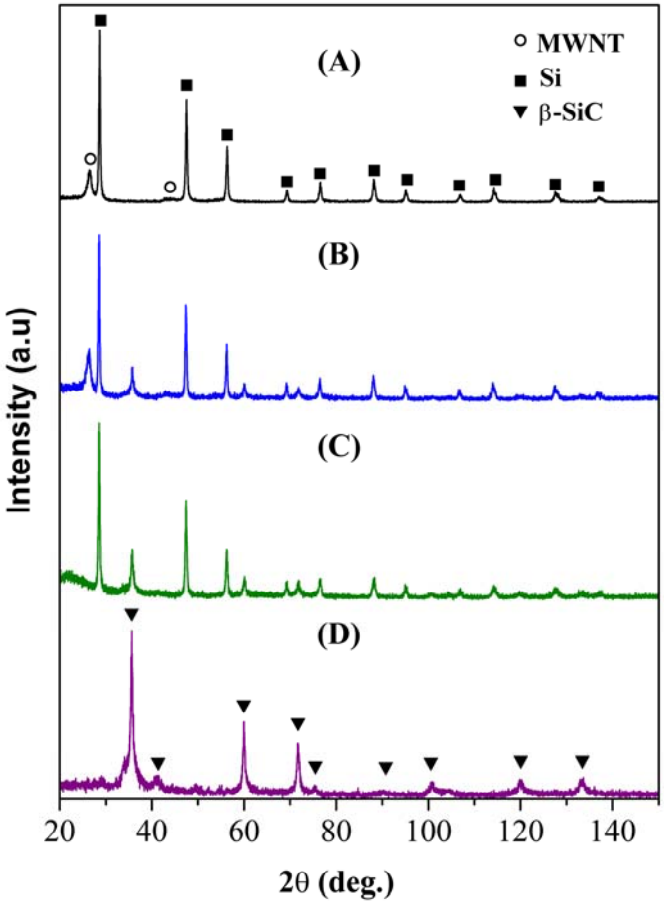

Fig. 3.1. XRD of samples: (a) initial mixture, (b) mixture sintered at 1473 K for 1 hour, (c) mixture sintered, and then oxidized at 1073 K for 1 hour, (d) samples after all treatments (sintering, oxidation, washing in KOH solution).

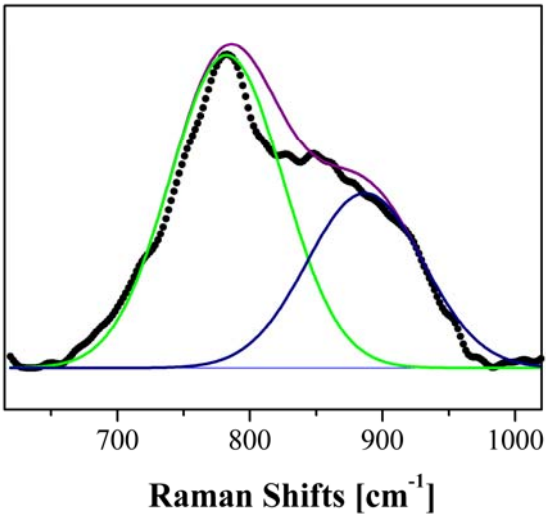

Fig. 3.2. Raman scattering spectrum of sample after all treatments.

III.1.1.2. Raman scattering spectra

Typical Raman scattering spectrum of obtained specimen is shown in Fig. 3.2, and the overlapping peaks were separated by Gaussian functions. We found two peaks located at around 782 and 890 cm^{-1} which can be assigned to the transverse optical (TO) mode and longitudinal optical (LO) modes at the *Γ*-point of the Brillouin zone of SiC. Bulk β-SiC crystal with a zincblende structure possesses two peaks located at 796 cm^{-1} and 972 cm^{-1} corresponding to the TO phonon mode and the LO phonon mode, respectively.[73] Obviously we observe the large red shift of 14 cm^{-1} for TO mode and 82 cm^{-1} for LO mode, and these large shifts of band locations are in good agreement with Huang et al. calculations.[74] They attributed these huge red shifts to structure defects, such as stacking faults, residual stress, surface disorder, and size confinement. XRD spectra also demonstrate the structure defects inside the sample.

III.1.1.3. TEM

Fig. 3.3 shows the typical TEM image of the mixture after sintering. It revealed that the mixture was almost the same as the initial mixture, and the structure and morphology of MWNTs were similar, and only minor difference was observed. The arrow in Fig. 3.3 points a thin and solid thread-like structure attached to the surface of

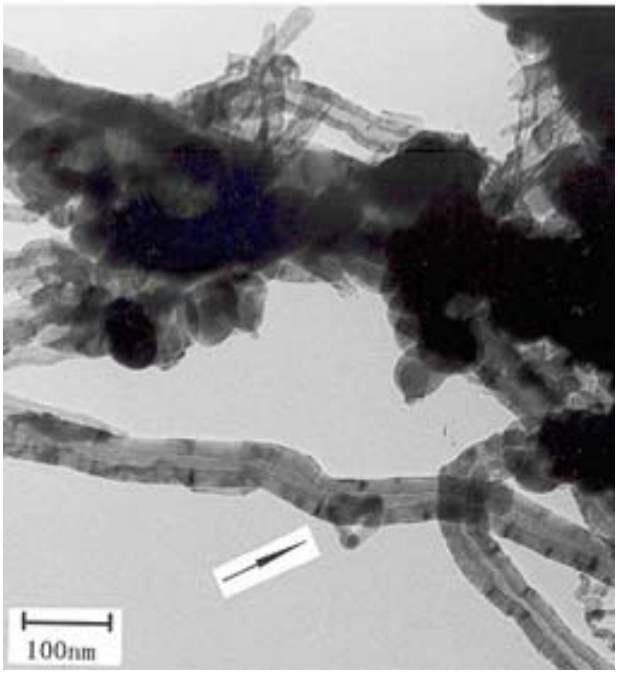

Fig. 3.3. Typical TEM image of mixture sintered at 1473 K for 1 hour.

MWNTs. With the assistance from the above-mentioned XRD, Fig. 3.1b, and Raman scattering spectra, Fig. 3.2, we assumed that these new growing thread-like structures were β-SiC. Fig. 3.4 shows the TEM image of the sample after sintering and oxidization. The MWNTs structures were absent from the sample, and this result matched quite well

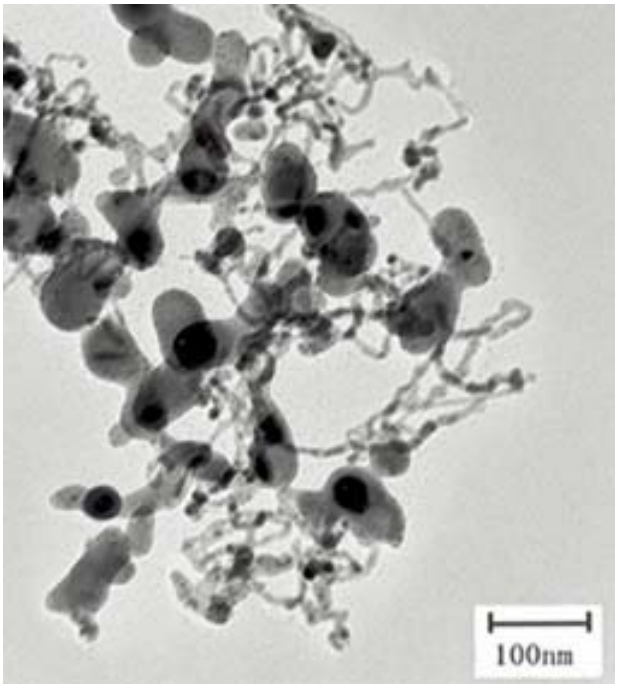

Fig. 3.4. Typical TEM image of mixture sintered, and then oxidized at 1073 K for 1 hour.

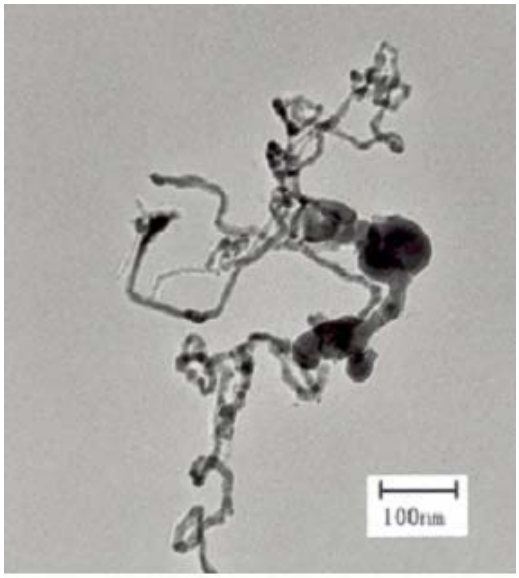

Fig. 3.5. Typical TEM image of sample after all treatments (sintering, oxidation, and washing in KOH solution).

the XRD, Fig. 3.1c. Lots of curved and randomly oriented nanothreads can be seen in this image. Usually ends of nanothreads are connected to SiC particles. The diameters of the nanothreads were uniform but their lengths varied from nanometers to tens of micrometers. Fig. 3.5 shows the TEM image of the sintered sample after oxidization and washing in KOH. Often one or both ends of threads were attached to large grains of SiC. Analysis of TEM images of β-SiC nanothreads showed that their diameters were around 20 nanometers. These diameters were distinctly smaller than those of starting MWNTs.

III.1.2. Silicon in liquid phase

In this experiment, the molar ratio of MWNTs and Si in mixture was 1:3. Two different sets of samples were made in the liquid region of Si. One sample, S2, was obtained by sintering the mixture at 1723 K for 1 hour in a conventional oven. Another sample, S3, was synthesized at 1723 K and 0.5 GPa using a piston-cylinder system. The cleaning procedure was similar as that described in the previous section with the exception that here we used stronger acid solution, a mixture of HF (10 wt. %) and HNO_3 (30 wt. %), to etch Si. We replaced KOH with the acid solution because after sintering, samples became very hard.

III.1.2.1. X-ray diffraction patterns

Fig. 3.6a shows the XRD patterns of the initial mixture of MWNTs and Si. All of the Bragg peaks (111), (220), (311), (400), (311), (422), (511) of Si in the range from 20^o to 100^o appeared, and the peaks were sharp and intense. For MWNTs, only one tiny

hump was observed at 26.53°. It corresponds to the (002) reflection. Other peaks were too small to be seen. Fig. 3.6b shows the XRD pattern of sample S2. Obviously, all of the Si Bragg peaks disappeared, and the new peaks can be indexed to the known β-SiC phase with lattice constant a = 4.348Å. The (002) peak of MWNTs did not change

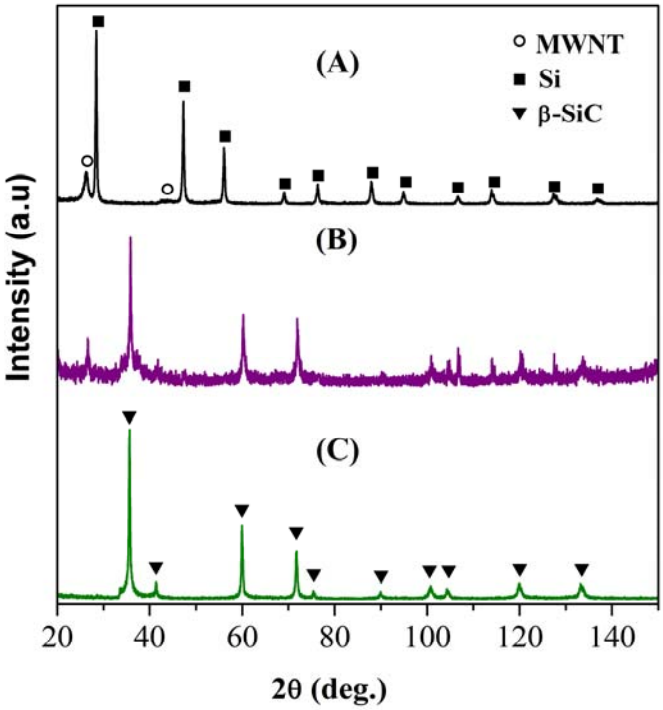

Fig. 3.6. XRD of samples: (a) initial mixture, (b) sample S2, (c) sample S3.

significantly. It indicates that β-SiC and MWNTs coexisted, but Si did not exist in sample S2. From this information, we may infer that the outer layer of carbon nanotube reacted with Si and converted into SiC layers that deposited on the core of carbon nanotube, so that the inner layers of MWNTs were prevented from oxidization by the grown SiC layers. It is the reason why MWNTs components were shown in the XRD

patterns. Fig. 3.6c shows the XRD patterns of sample S3. Obviously, the sample S3 is only pure β-SiC and did not include any MWNTs. Compared to Fig. 3.6b, the Bragg peaks of SiC in S3 were sharper and stronger. We can explain it by the differences of the grain sizes and the residual stresses in two samples. Except for the reaction pressure, all conditions were similar for S2 and S3. However, the results were quite different indicating that the applied pressure in the synthesis process had an important effect on the composition and structure of the final products.

III.1.2.2. Raman scattering spectra

Fig. 3.7a and Fig. 3.7b show Raman spectra for samples S2 and S3, respectively. In both spectra, there are two peaks centered at 792 cm^{-1} and 966 cm^{-1}, which correspond to the TO and LO phonon modes at the Γ-point of the Brillouin zone of β-SiC. In addition, three other peaks located approximately at 1350 cm^{-1}, 1580 cm^{-1}, and 1610 cm^{-1} which are the D, G, and D' bands of MWNTs, were clearly observed in Raman spectra of S2, but not for S3. These results matched very well those of the above XRD, and confirmed that in S2 SiC and MWNTs coexisted, while S3 was pure SiC.

We also investigated Raman spectra of S2 under high pressure up to 5 GPa. The high-pressure measurements were carried out at room temperature using a 514 nm laser and a gasketed diamond anvil cell. The hydrostatic pressure dependence of the TO and LO phonons frequencies of bulk SiC was investigated by Olego and Cardona.[75, 76] They observed that with increasing pressure these frequencies shifted toward higher values. Our studies confirmed these results. As expected, we did not observe any indication of a

possible phase transition. With increasing pressure the peaks significantly broaden and the peak maxima shift.

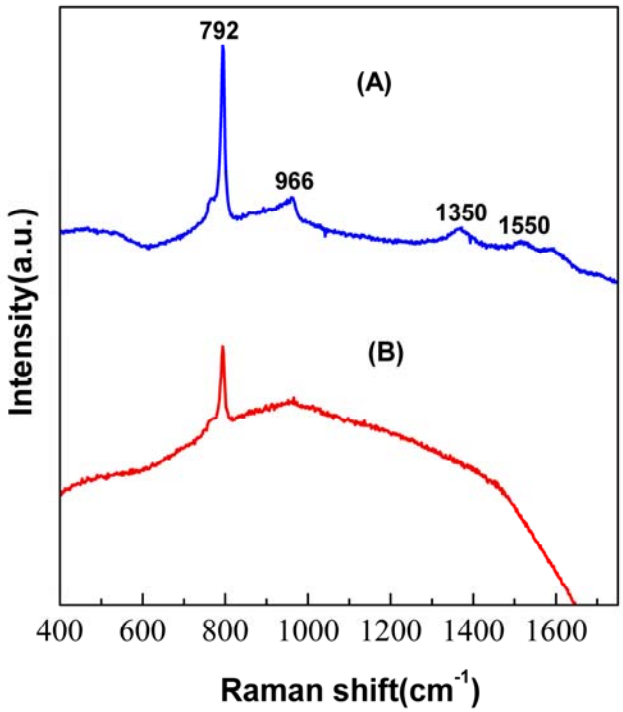

Fig. 3.7. Raman scattering spectra of samples: (a) sample S2, (b) sample S3.

III.1.2.3. TEM images

Fig. 3.8 shows the TEM image of sample S2. The shapes of the synthesized nanofibers were irregular and the surfaces were much rougher than the surface of carbon nanotubes. Another worthnoting phenomenon was that the diameters of the grown structures ranged from 70 to 105 nm and were larger than the size of MWNTs. It appears that SiC grew on individual MWNTs. Once the MWNTs were coated with SiC, it prevented further reaction leaving inner layer intact. TEM of sample S3 showed irregular

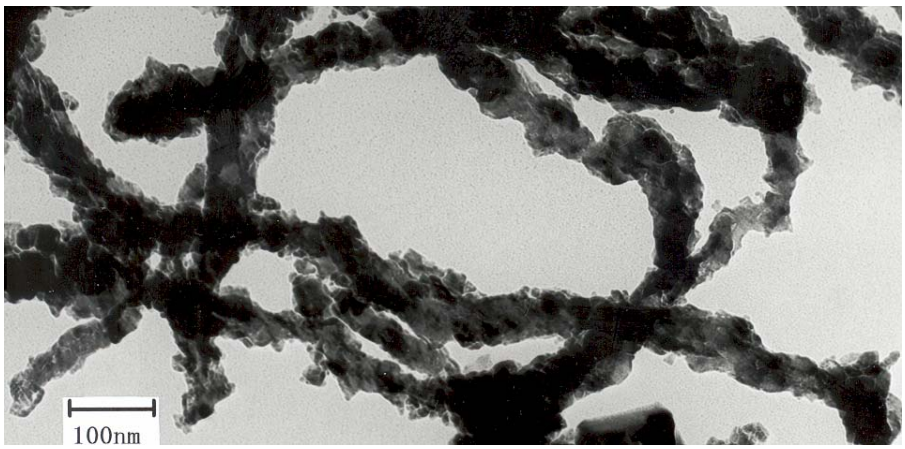

Fig. 3.8. Typical TEM image of sample S2.

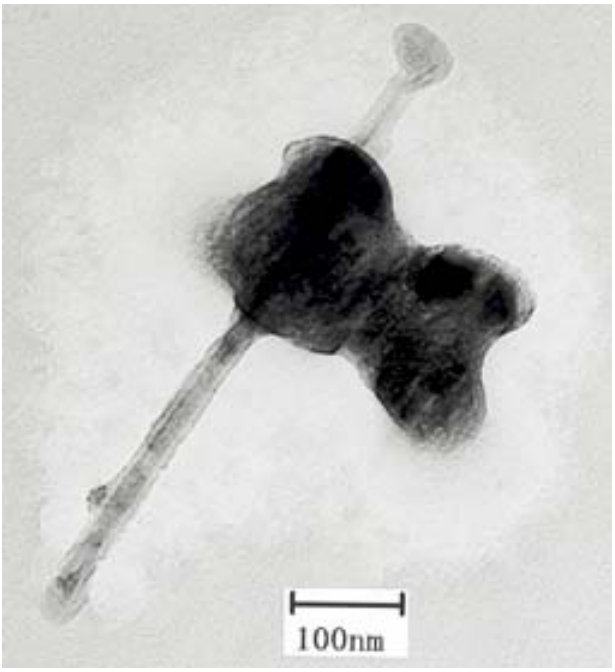

Fig. 3.9. Typical TEM image of sample S3.

nanoparticles mixed with few nanorods. The diameters of SiC nanoparticles ranged from 30 nm to 150 nm. The nanorods shown in Fig. 3.9 were thinner than the starting MWNTs.

III.1.3. Composition of SiC sintering in silicon solid and liquid

At normal pressure the melting point of Si is at 1688 K[77], and the structure of carbon nanotubes may not be lost below 3273 K.[78, 79] Therefore, S1 was made at temperature lower than the melting point of Si while S2 and S3 were synthesized through the liquid Si reaction with CNT.

Here we start with the unique structures of CNTs to explain their solid-state reaction with Si. CNT is graphene sheet seamlessly wrapped into a cylindrical tube. Most of carbon atoms in graphene sheet are linked into rolled layer of hexagons through sp^2 hybridization. Besides the hexagonal structures, also pairs of adjacent (7, 5)-(5, 7) rings, so-called Stone-Wales (SW) defects, are intermingled, as shown in Fig. 3.10. The

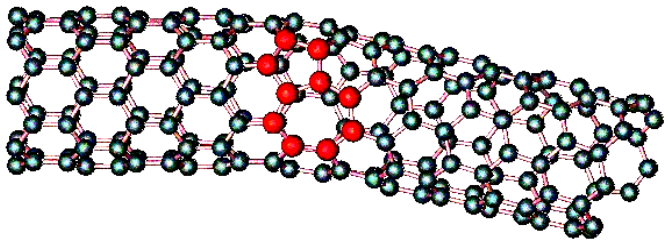

Fig. 3.10. Atomic structure of CNT. The red balls denote the atoms forming the (7, 5)-(5, 7) rings

SW defects are formed unavoidably during nanotube synthesis process, since additional paring heptagon with a pentagon is energetically favorable and can close up the curved structure of CNT. The SW defects are believable to have a pivotal role in defining the properties of CNT.[80, 81] It is generally accepted that SW defect sites trigger and impel chemically the reaction of CNT with other materials.[82, 83] In our case, under high temperature, SW defects can glide, twist and distort, thereby some C-C bonds may break. It is then energetically favorable for these dangling bonds to react with Si atoms. Here, we have only considered the SW defects. In addition to SW defects, the larger spacing among the cylindrical layers of CNT may lead to uncorrelated atomic positions and the loose connection makes C-C bonds break easily and react with Si.

Sample S1 was composed of SiC nanothreads and spherical particles of diameters varying between 10 to 60 nm. The fact that SiC exists in the form of two distinctly different structures suggests that they could have been formed in the course of two different reactions. We postulate that spherical particles were formed after the collapse of carbon nanotubes to form carbon atom clusters of different sizes and number of layers. The hollow and long cylindrical structures disappeared and in their place grew curled, onion-like graphitic structures composed of concentrically nested graphene planes. The high curvature of the graphitic shells and dangling bonds facilitated reaction with silicon. The size of the produced particles depended on the size of collapsed carbon nanotubes. Carbon nanotubes used in the reaction had sizes between 60 and 100 nm, but these were hollow structures and after collapse smaller sizes were expected. Most of the spheres had diameters close to 60 nm, but we also found chains of smaller spherical nanocrystals, 10

nm to 20 nm in diameter. Silicon carbide nanothreads had diameters close to 20 nm. Their morphology indicates that they were obtained as a result of a carbon nanotube confined reaction. It is possible that after a C-C bond breaks, silicon and carbon atoms can form Si-C bonds which constitute a nucleus for further SiC crystal growth along carbon nanotubes. This scenario explains growth of straight SiC rods from straight sections of MWNT. This was a solid-state reaction as silicon was in the solid phase. Analysis of XRD line shapes can provide information on the size of nanocrystallites. The estimates based on the Scherer's method indicated that along the [111] directions the crystallites were 18 nm long and along the [220] direction about 25 nm. Presence of small nanocrystallites was also confirmed by a red shift of Raman LO and TO phonon peaks. The magnitudes of the shifts are significant. Significant modifications in Raman spectra, including frequency shifts, were observed when crystal sizes were reduced to below 20 nm. Due to large error I did not evaluate the relationship between crystallite size and frequency shift. However, the shifts measured in this study were significantly indicating that the crystallite sizes were small, probably less than 20 nm. Asymmetry of XRD peaks could be associated with the presence of stacking faults. This assumption was confirmed by the presence of the 765 cm^{-1} shoulders in all Raman spectra. This shoulder could be regarded as arising from extensive stacking faults within crystallites. We also concluded that the population of stacking faults in specimen was very high, and it varied from one location within the sample to another. This conclusion is based on the fact that the shoulder's position relative to the TO center was different for various points on the surface of specimen. The origin of the different distribution of stacking faults

within sample S1 is in its manufacturing protocol. This sample was obtained at a relatively low temperature, below the melting point of silicon. The SiC nanowires obtained had diameters of about 20 nm and often exceeded lengths of 500 nm. TEM images show straight nanowires along with twisted and entangled threads of similar diameter. In such diverse structures abundant stacking faults of non-uniform distribution could exist. It is important to add that when we repeated the experiment using the same conditions, but the mixture of MWNT and silicon powder was loose and not in the form of compressed pellets, the efficiency of the reaction was very poor and only traces of SiC were detected. Clearly, the success of the reaction depends on close proximity of silicon particles and MWNT.

In the case of sample S2, Si became liquid and it is plausible to assume that it covered the outside surface of carbon nanotubes. TEM images indicate that the sample consists of C – SiC coaxial nanotubes, namely carbon nanotubes coated with nanosize SiC in the form of tiles. These tiles have different shapes, sizes, and orientations and partially overlap. Such morphology is expected for a product of a reaction with a significant number of nuclei; i.e. the SW defect sites on the surface of CNT. Once nanocrystallites covered the outer surface of carbon nanotubes, the reaction could proceed further only when carbon atoms from MWNT diffused through SiC toward silicon, or silicon atoms diffused toward the nanotubes. It is reasonable to assume that diffusion paths through grains require higher activation energy than paths through grain boundaries. Such mechanism would facilitate tile-like growth of SiC. XRD and Raman spectrum verified that we produced coaxial structure of carbon nanotubes (inside) and

SiC (outside). The diameters of products were bigger than those of starting MWNTs, however, their basic shapes were similar. Their morphology and composition imply that they were obtained as a result of a carbon-nanotube confined reaction, with MWNTs used as templates. Applying the Scherrer method to x-ray diffraction spectra we obtained 30 nm for the size of crystallites, in good agreement with the dimensions of the tiles estimated from the TEM images in Fig. 3.8. This result indicates that the SiC tiles were composed of crystallites whose boundaries were defined by defects. The splitting of Raman spectra of nanowire S2 increases rapidly with increasing pressure and at about 5 GPa it approaches the value observed for bulk SiC. Apparently, the structure of surface layer is altered by increased pressure. Indeed, high pressure x-ray diffraction measurements conducted for nanosize SiC powder indicated that the surface layer had an expanded structure with lattice constant slightly larger than that for the bulk crystal.[84] But as pressure was increased the lattice constant of the surface layer decreased at a faster rate than that of the interior and at pressures above 3 GPa there was practically no difference in lattice parameters of the surface layer and the core. A more rapid compression of outer layers for nanowires would explain increased splitting between the LO and TO bands and when the compression of both the surface layers and the core were similar the splitting approached the value observed for bulk material.

When initial mixture was sintered at 1723 K and 0.5 GPa, the products, sample S3, consisted of irregular particles and small concentration of nanorods. Most of MWNTs may lose their hollow and long cylindrical structures during reaction. We postulate that irregular particles were formed after the collapse of carbon nanotubes. The

tube-like structures collapsed to form carbon atom clusters of different sizes and number of layers. The hollow and long cylindrical structures disappeared and in their place grew curled, onion-like graphitic structures composed of concentrically nested graphene planes. The high curvature of the graphitic shells and dangling bonds facilitated reaction with silicon. The size of the produced particles depended on the size of collapsed carbon nanotubes. Some surviving carbon nanotubes may react with liquid Si atoms to form SiC nanorods. The products were pure SiC, which was confirmed by x-ray and Raman spectra.

III.2. Kinetics of CNT-silicon reaction under HTHP

In III.1, we investigated the CNT-Si reaction under high temperature and ambient pressure. It showed that at different temperatures the as-grown SiC possessed dissimilar shape and morphology. However, we still do not know how the reaction took place between CNT and Si and whether it was easy or difficult to form SiC from CNT, compared to diamond and graphite. In this section we present the kinetics study between the CNT and Si.

All the carbon phases, graphite, CNT, and diamond, can react with Si to form SiC, which is an important material and plays a key role in many fields. Sustained efforts have been devoted to studying the reaction between elemental carbon and Si. Gorovenko et al.[85] investigated the high-temperature interaction in the silicon-graphite system. They found that the activation energy for the reaction between Si and graphite was around 220 kJ/mol and the process was limited by diffusion of carbon in liquid silicon. Previously,

our group studied kinetics of SiC formation from diamond and Si under high-temperature and high-pressure conditions. We concluded that the reaction was controlled by the diffusion of carbon atoms through the newly formed SiC layer with activation energy ranging from 170 kJ/mol for nano-diamond to 260 kJ/mol for micro-diamond.[86] To the best of our knowledge no information on the reaction between CNT and Si is available.

III.2.1. Sample preparations

The starting material was the mixture of CNT and Si in 1:1 molar ratio, and the details of preparing of initial mixtures were given in chapter II. All samples listed in Table 3.1 were fabricated by high-pressure sintering technique. X-ray powder diffraction

Table 3.1. Sintering conditions of samples.

Temperature [K]	Pressure [GPa]	Sintering time [s]
1270	2.0	60, 180, 300 540, 780
1320		60, 180, 300 540, 780
1370		60, 180, 300, 540, 780, 1020

was used to measure the degree of reaction, and the activation energy of SiC formation from CNT was determined by fitting the reaction rates to Avrami-Erofeev model.

Meanwhile, the domain sizes and microstrains of the SiC phase were characterized through the analysis of the shapes of x-ray diffraction lines.

III.2.2. Results

We selected three sintering temperatures, 1270 K, 1320 K, and 1370 K. Under 2 GPa, all three temperatures are below the melting point of silicon. During the reaction, both silicon and CNT were in the solid state. Attempts to study the reaction at a lower temperature, 1170 K, failed because in a reasonable time we were able to collect SiC insufficient for further analysis. At 1470 K the process was very fast and it was impossible to control the reaction. In both cases experimental errors prevented us from determining reaction rates. Normally, good quality diamond-SiC composites are manufactured in the stable region of diamond under pressure above 5.0 GPa. Recently, it has been suggested that good quality diamond-SiC composites could be produced at a lower pressure, even as low as 2 GPa.[87] X-ray diffraction patterns were recorded for all specimens, an example is shown in Fig. 3.11. Characteristic peaks of Si, SiC and CNT can be clearly observed indicating that the reaction was incomplete. Only one phase of the cubic SiC, also called the β phase, was detected. For each run the amount of SiC was determined from the intensities of peaks of Si (111) and SiC (111) by using calibration curves obtained from x-ray diffraction patterns of known quantities of SiC and Si. Here we consider Si (111) and SiC (111) peaks only, because (111) reflections of Si and SiC give rise to stronger peaks than others and larger intensity peaks provide more accurate determination of the quantities of Si and SiC. When other peaks were used to estimate

the quantity of SiC similar results were obtained; however, the error margins were greater, and these results were not included in further analysis. This results confirms that the specimens did not undergo texture evolution in the temperature region investigated. The degree of reaction α(t) for each independent run was calculated using Eq. 2.27. The plots of α (t) vs. t are shown in Fig. 3.12. The solid, dash and dot lines represent the best Avrami-Erofeev fittings of α(t) for three different temperatures. The fitting parameters m and k of the Avrami-Erofeev equation are listed in Table 3.2.

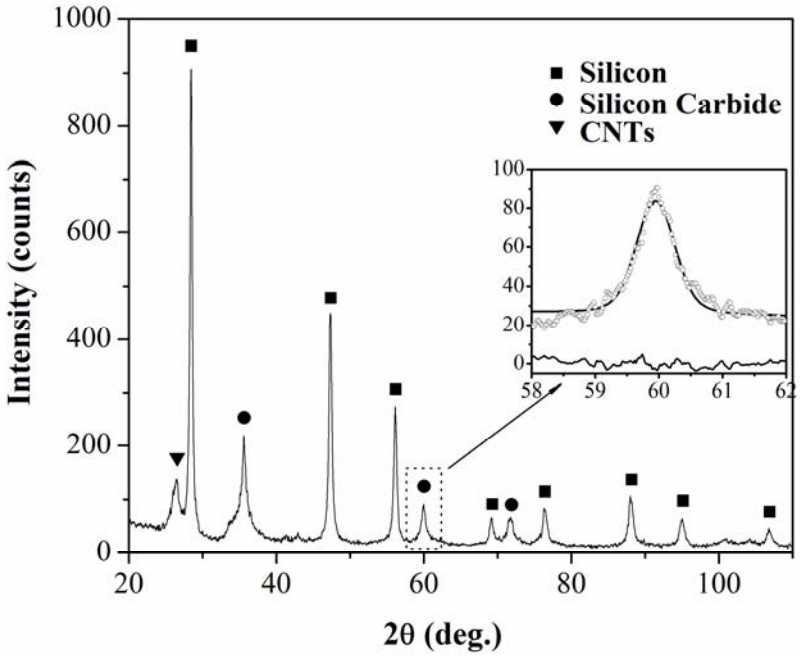

Fig. 3.11. X-ray diffraction pattern of sample obtained at 2 GPa, 1370 K and sintered for 60s. The insert represents measured (open circles) and fitted (solid line) diffraction profiles of SiC (220) using the Voigt function, and the difference between the two sets of curves is shown in the bottom part of the insert.

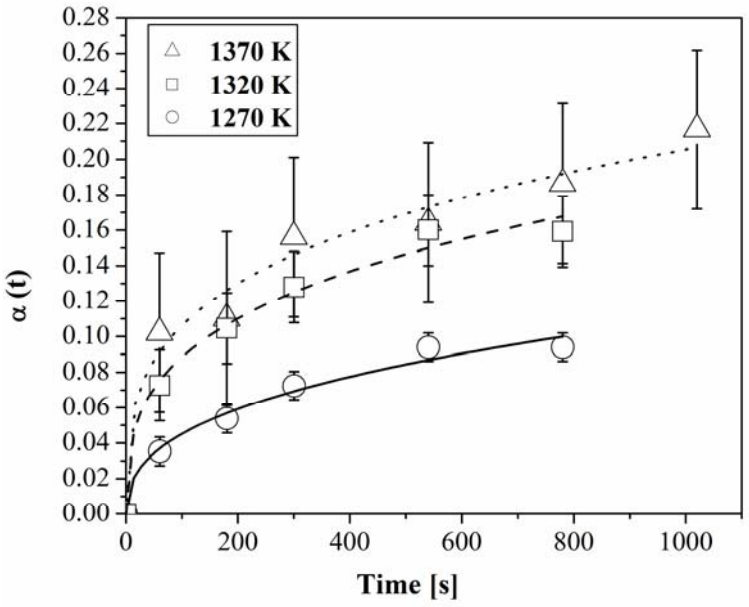

Fig. 3.12. Plot of degree of reaction, α, vs. time. Solid, dash, and dot lines represent the best fit of the Avrami-Erofeev equation to experimental data for the (111) reflections at 1270 K, 1320 K, and 1370 K, respectively.

Table 3.2. Kinetics parameters of Avrami-Erofeev model obtained by fitting experimental data to equation 2.25.

T [K]	k (10^{-6}) [s^{-1}]	Δk (10^{-6}) [s^{-1}]	m (10^{-1}) [-]	Δm (10^{-2}) [-]
1270	4.67	3.52	4.01	4.84
1320	7.78	4.84	3.32	3.54
1370	9.00	6.66	3.12	4.23

According to the Arrhenius law, the reaction rate constant is represented by the equation:

$$k = A \cdot \exp\left(-\frac{E}{R \cdot T}\right) \tag{3.1}$$

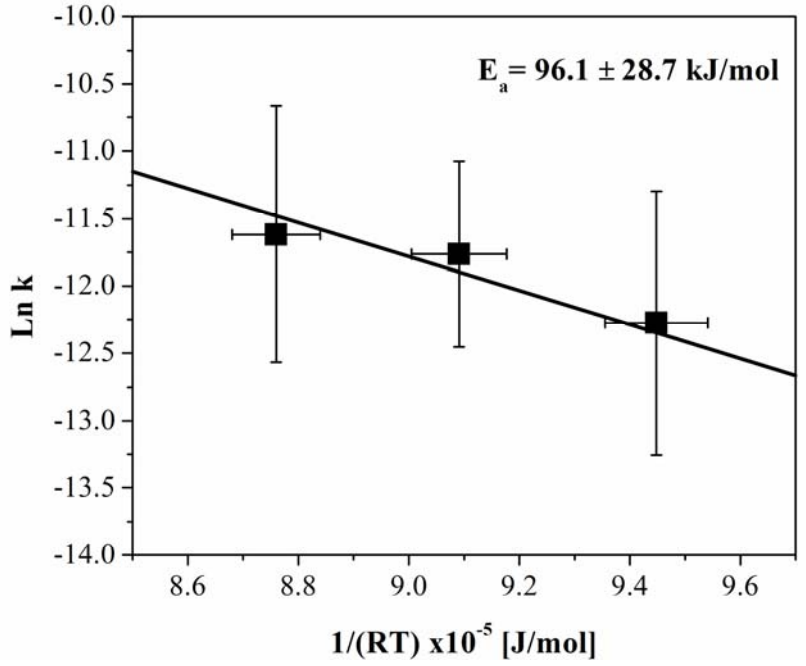

Fig. 3.13. Arrhenius plot of the reaction rate constant k against reciprocal temperature.

Where R is gas constant and A is called the frequency factor. A plot of ln k as a function of reciprocal temperature is shown in Fig. 3.13. The activation energy for solid-state reaction between Si and CNT under 2 GPa is 96.1 ± 28.7 kJ/mol, estimated from fitting the data to a straight line. This value is smaller than that for SiC manufactured from diamond [86] or graphite [85].

For domain sizes and microstrains of as-grown SiC, our analysis focused on (111) and (220) peaks of SiC. Other peaks were not taken into consideration due to their lower intensities which may cause unexpected errors in calculations. Both peaks were

refined by the double Voigt multiple-line integral-breadth method, and one example of the refined (220) peak is shown in the insert of Fig. 3.11. Using (111) and (220) peaks as

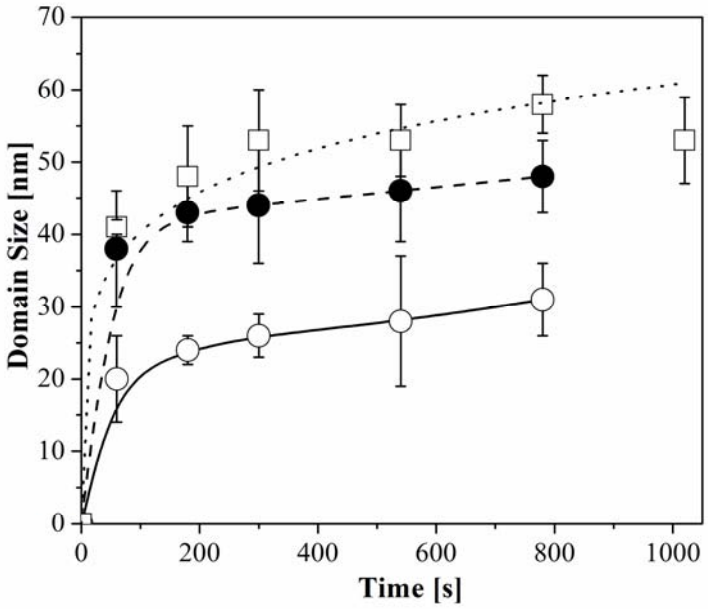

Fig. 3.14. Plot of domain size of as-grown SiC. ○, ●, and □ represent the experimental data obtained at 1270 K, 1320 K, and 1370 K, respectively. Solid, dash, and dot lines represent the best fit of experimental data obtained at 1270 K, 1320 K, and 1370 K, respectively.

input profiles, the domain sizes and microstrains of as grown SiC have been derived, and the results are shown in Fig. 3.14 and Table 3.3. At a similar sintering time, the higher temperature resulted in larger grain size. At a constant temperature the average grain size initially increased, but with elapsed sintering time this growth process slowed down and eventually stopped. The microstrains inside the as-fabricated SiC are listed in Table 3.3.

It is seen that the dislocation population decreases with the sintering time. As expected, higher temperature leads to a smaller concentration of defects.

Table 3.3. Microstrains inside the as-fabricated SiC.

Sintering time [s]	ε (10^{-4}) at 1270 K	ε (10^{-4}) at 1320K	ε (10^{-4}) at 1370 K
60	62 ± 16	58 ± 16	38 ± 4
180	51 ± 17	32 ± 13	37 ± 4
300	49 ± 20	48 ± 16	35 ± 3
540	45 ± 12	25 ± 12	35 ± 3
780	47 ± 16	48 ± 18	22 ± 3
1020			29 ± 2

III.2.3. Discussion

The activation energy of SiC formation from CNT and Si is lower than the reported values for reactions when carbon was in the form of diamond or graphite. We may trace this phenomenon back to their different atomic structures of the precursors. Diamond is sp^3-hybridization of carbon, and a three-dimensional (3D) network is formed by binding the tetrahedral unit structures together. The bond between two atoms in diamond crystal is very strong. In graphite the sp^2 hybridization results in strong C─C bonds within grapheme layers. A perfect CNT is graphene sheet seamlessly wrapped into a cylindrical tube. Experimental results however clearly indicate that CNT possess many defects. As discussed before, the most common defects in CNT are SW defects. In our

case, under high temperature and high pressure conditions CNT are compressed and thus the number of defects probably increased. We hypothesize that a high SW defect concentration in CNT is critical to lower the activation energy. Of course, other defects, such as vacancies, impurities, and kinks, may also be present and their combined effect further lower the activated energy.

We assume that the reaction with silicon starts at SW defects on outer walls of multiwall CNT. Then SiC grows along the tube outer walls but also radially. A high density of defects results in numerous nucleation sites. As the grains grow they overlap and coalesce. The average size of SiC domains varies between 20 and 50 nm. Of course, continuing the reaction for an extended period of time at increasingly higher temperature facilitates growth of the crystallites. But with sintering time elapsed, as the thicker SiC layers impedes the penetration of atoms, the SiC grain growth is hindered. As expected, analysis of x-ray diffractograms indicated that an additional benefit of conducting the reaction at high temperature is an annealed structure with a dramatically reduced population of strains.

Zhao *et al*[7] showed experimental evidence that reduction of the average size of SiC crystallites from tens of microns down to about 20 nm increased the fracture toughness of diamond/SiC composites. They claimed that the nanosize SiC matrix would decrease the ability of cracks to propagate, and this mobility reduction thus leads to an improvement of the fracture toughness of the composites. They also showed that a lower population of dislocations enhances the hardness of the SiC matrix in which diamond crystals are embedded.

The results of this study indicate that a nanostructured SiC matrix could be realized by a reaction between silicon and CNT. The nanosize crystallites and low strains of as-fabricated SiC could improve mechanical properties of composites. In the next chapter, we mix diamond crystals with a silicon/CNT mixture and conduct high temperature sintering of diamond based composites at pressures higher than 5 GPa.

In summary, the solid-state reaction between CNT and Si has been investigated under high pressure and high temperature. We focused on the kinetics study and microstructure analysis. Our results demonstrate that CNT may have higher chemical reactivity than other forms of elemental carbon, which could be ascribed to the Stone-Wales defects on CNT surface. X-ray analysis shows that higher temperature created larger size grains with low strains. Our results are of long-term application significance because they demonstrate that CNT could be used to design and develop CNT-SiC nanocomposites with strong nanocrystalline bonding matrix and, conceivable, with both enhanced fracture toughness and supper hardness which could be applied in harsh environments.

IV. CNT based diamond composites

IV.1. CNT/SiC nanocomposites synthesis and characterization

In the previous section we listed the lower activation energy of SiC formation from CNT and Si. In this section we characterize SiC sintered from CNT and Si under high P-T conditions. Forming strong bonds between Si and C atoms is the primary requirement to produce hard composites.

The starting materials were similar to those discussed in the previous section, but the weight proportion was changed and we used the ratio of 3:2 of Si nanocrystals to CNTs. Samples were synthesized at pressure 2 and 8 GPa, and temperature 1770 K and 1970 K, under which Si crystals were melted completely and reacted with carbon atoms to form SiC. X-ray photoelectron spectroscopy (XPS) spectra were recorded using Multitechnique Electron Spectrometer PHI 5700/660 from Physical Electronics. The XPS spectra were analyzed using a Multipak program from Physical Electronics.

IV.1.1. Results

X-ray diffraction patterns of the initial Si-MWNT mixture and selected composites are shown in Fig. 4.1. The x-ray diffraction peaks of SiC demonstrate significant line broadening, comparable to that of initial silicon powder. X-ray diffraction patterns of composite samples sintered at 8 GPa have been refined by the double Voigt multiple-line integral-breadth method. Volume-averaged crystallite size and microstrains were estimated using BREADTH program. The results are listed in Table 4.1.

XPS scans reveal presence of carbon, silicon, and oxygen. The carbon C1s peak has clearly two components, one at 284.4 eV another at 283.5 eV, Fig. 4.2. These binding energies are indicative of graphitic like systems and SiC, respectively.[88] From Fig. 4.1 it is seen that relative intensity of the SiC peak increased with pressure. Samples prepared at the low pressure region, see Fig. 4.2, have silicon Si2p peak composed of two bands, one centered at about 101.3 eV (due to SiC), another at 103.5 eV (8 GPa) or 104.7 (2 GPa) eV (identified as due to SiO_2). At certain locations on the surface of the specimen sintered at 2 GPa there was also a small peak at about 99 eV due to crystalline

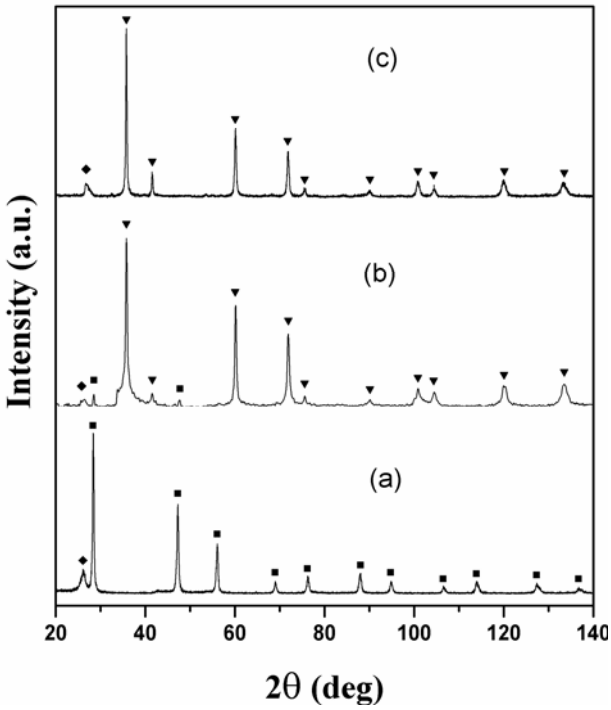

Fig. 4.1. XRD of the initial Si-CNT mixture (a), and SiC-CNT samples sintered at T = 1770 K and 2 GPa (b) and 8 GPa (c). Squares — reflections due to silicon and CNT; Triangles — reflections due to SiC.

silicon.[88] In the spectra obtained for the specimens sintered at 8 GPa the SiC peak was strong and other two components were negligible small. The oxygen O1s peaks were detected for all composites and had similar binding energies and band shapes, are not shown here. It is worth noticing that intensities of the oxygen peaks were small for the 8 GPa specimens. For the XPS measurements all samples where placed inside the vacuum chamber and mechanically broken under ultra high vacuum conditions into two segments and the freshly uncovered surfaces were never exposed to the atmosphere. To be sure that observed spectra are due to atoms chemically bonded to the composite and not physically adsorbed to the surface, spectra were recorded before and after the specimens were sputtered for 2 minutes by Ar ions with the energy of 1 keV. No changes in band positions were observed. It is very likely that the specimens broke where their structure was the weakest, probably where the concentration of silica and/or nanotubes was high. Therefore, intensities of bands measured by the XPS technique do not necessarily provide information on the composition of the body of the specimens, but rather are limited to the exposed surface. The Raman spectrum of one of specimens sintered at 8 GPa is shown in Fig. 4.3. A broad peak at 794 cm^{-1} corresponds to the transverse optic (TO) phonon mode at the Γ-point of the SiC Brillouin zone.[89] This peak was broad and asymmetric. Longitudinal optic (LO) phonon peak of SiC was completely suppressed when the 780 nm excitation line was used. The LO band has its intensity dependent on the wavelength of the incident laser, this effect has been discussed in detail in our previous report.[90]

Table 4.1. SiC phase structural parameters, hardness, and fracture toughness of SiC-CNT composites sintered at the pressure 8 GPa and different temperatures.

Sintering temperature, [K]	SiC structural parameters		Vickers hardness H_V, [GPa] (P = 4.9N)	Fracture toughness K_{IC}, [MPa·m$^{0.5}$]
	$\langle x \rangle_{vol}$, [nm]	ε, %		
1770	37 ± 5	0.4	21 ± 2	7.1 ± 0.9
1970	34 ± 6	0.4	20 ± 2	6.8 ± 0.8

Close to the resonance, when the 514 nm laser excitation line carrying the energy close to that of the band gap energy of 2.4 eV was used, the LO band appeared at about 964 cm^{-1} and had its intensity similar to that of the TO band.[90] Unlike for XPS, no traces of unreacted silicon were found in Raman spectra of all specimens. Two strong Raman peaks at about 1558 cm^{-1} and 1345 cm^{-1} were identified as due to MWNT.

Hardness and fracture toughness of samples are shown in Table 4.1. Sample sintered at 2 GPa were too soft to be measured. At 8 GPa, no substantial influence of the sintering temperature on the composite properties has been observed. Differences in hardness and fracture toughness values of the samples sintered at different temperatures were within the corresponding error margins.

IV.1.2. Discussion

Assuming that all the silicon and carbon had reacted, the composites should contain 86 wt. % SiC, leaving about 14% of the carbon unreacted. From XRD we found that most of the unreacted carbon was in the form of MWNT, although we cannot

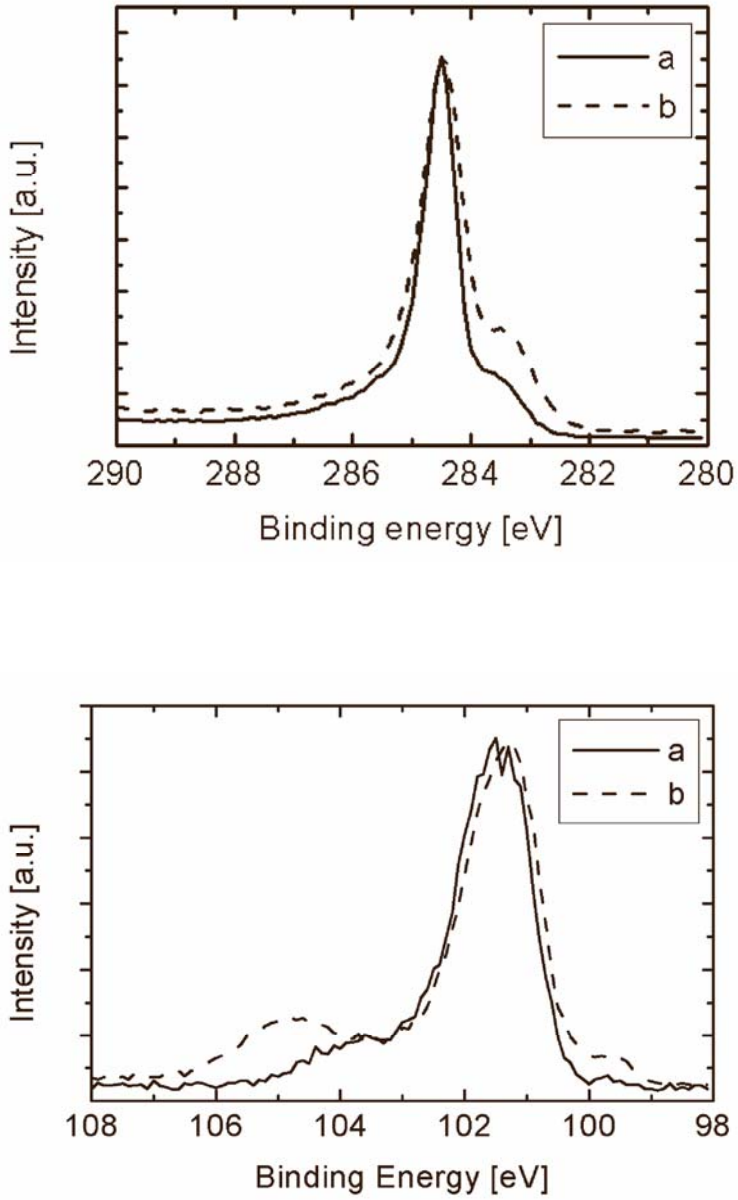

Fig. 4.2. XPS spectra of composites sintered at 1770 K and 2 GPa, broken line, and 8 GPa, solid line. Top — C1s region, Bottom — Si2p region.

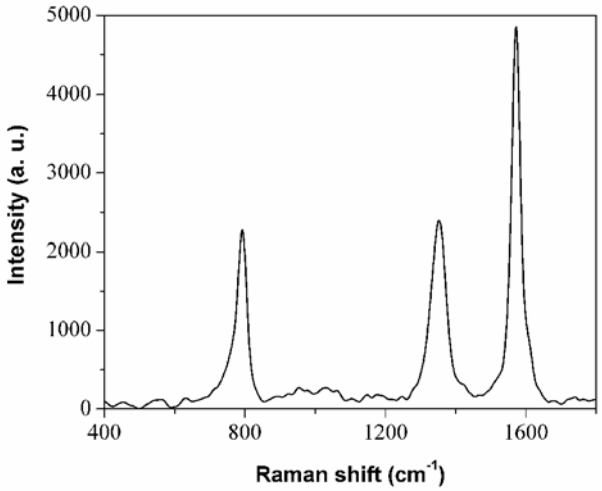

Fig. 4.3. Raman spectrum of the SiC-CNT sample sintered at 8 GPa and 1770 K, after background subtraction. 780 nm laser was used as an excitation light.

exclude the possibility of the presence of amorphous carbon. X-ray diffraction peaks indicate that carbon nanotubes survived high pressure treatment. This result is similar to that obtained by Munoz et al. who synthesized SiC nanorods by placing CNT between silicon wafers and heating them up to 1270 K.[91] Of course, concentration of the residual carbon depended on the sintering conditions and from XPS and XRD studies it was obvious that in specimens manufactured at 2 GPa there was less SiC than in samples prepared at 8 GPa. At the present time we cannot explain the effect of pressure on the efficiency of the reaction. We have not observed a similar trend during the manufacturing of diamond-silicon carbide composites.[92]

Analysis of XRD peak profiles has shown that the SiC phase of the composite has pronounced nanocrystalline structure: its volume-averaged crystallite size is in the range 32-37 nm. The large broadening of the Raman TO phonon peak (the line width at half

maximum is 20 cm^{-1}) may be attributed to both phonon confinement in nanocrystals and lattice imperfections.[90, 93, 94]

Similar structural parameters of the SiC phase for composites sintered at 8 GPa and 1770 and 1970 K indicate the absence of noticeable recrystallization in the temperature interval studied. This observation can be explained by the recrystallization restraining role of both nanotubes[95] and high pressure. It is worth noticing that nanoceramics sintered by other methods[96] showed a pronounced recrystallization tendency.

The composites obtained at 2 GPa were soft and we could not measure their hardness or fracture toughness. Their density was about 1.20 $g \cdot cm^{-3}$. As seen in Fig. 4.4, the surface was porous and contained randomly distributed MWNT. Also, the presence of oxygen, mainly in the form of silica, but also in various C-O and C-O-Si bonds, further weakened the composite. However, when the reaction was conducted at 8 GPa we found that the concentration of oxygen was much lower. In the cylinder-piston-type cell used during the low pressure sintering we employed talc as an insulating material. At high temperatures, the talc released water and oxygen, which subsequently reacted with the mixture inside the high pressure cell. The lack of oxygen in specimens obtained at 8 GPa is a result of the configuration of the toroidal cell, which did not require talc. We could not quantify the amount of oxygen from XPS intensities. XPS probes only the surface of the specimen, not its interior. Elemental analysis was also not conclusive; the specimens

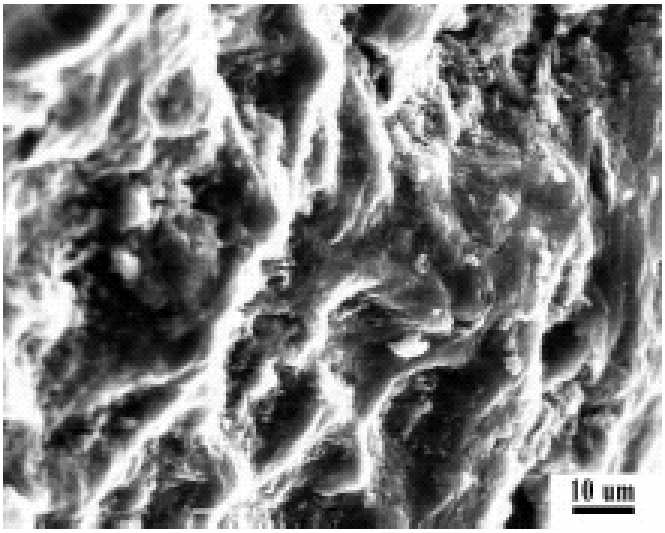

(a)

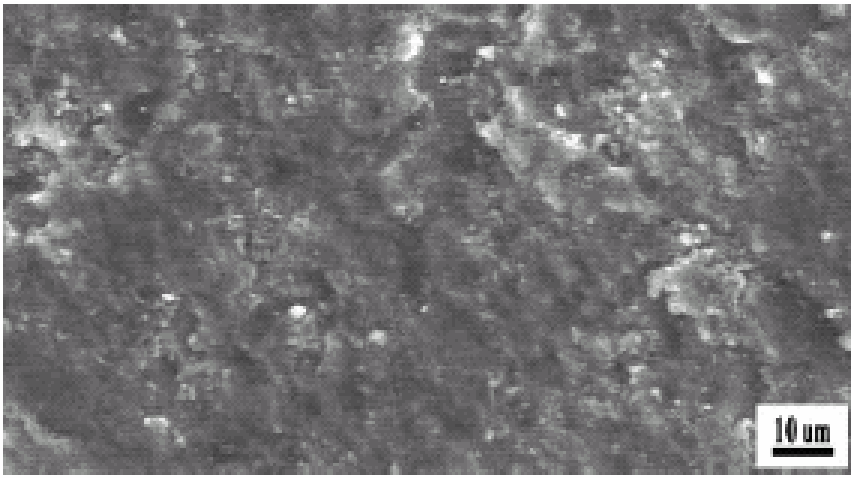

(b)

Fig. 4.4. SEM images of ruptured surfaces of specimens obtained at 1770 K and (a) 2 GPa and (b) 8 GPa. Agglomerates of silicon carbide coated MWNT can be recognized in (a).

were very hard and difficult to completely pulverize. The high hardness of composites sintered at 8 GPa is also a result of the lack of graphite.

The density of the composite samples produced at 8 GPa, 1.40 $g \cdot cm^{-3}$ is greater than the density of specimens obtained at 2 GPa, 1.20 $g \cdot cm^{-3}$, which is probably a result of the lower porosity of the samples obtained at higher pressure; compare the SEM images shown in Fig. 4.4. These samples have relatively high fracture toughness, which may be attributed to the reinforcing properties of carbon nanotubes. The reaction between Si and CNT should proceed faster at defects of the outer shells, resulting in uneven penetration of the growing SiC crystals into the multiwall carbon nanotubes. In addition, nonuniform distribution of silicon around CNT contributed to this effect. As a result, the unreacted interior of the nanotubes, which remain in the composite, should be interlocked with the silicon carbide nanocrystalline matrix. Such structure will provide an effective mechanism of stress transfer between the composite phases.

The strong bonding between Si and CNT under higher pressure, 8 GPa, indicates that it is possible to manufacture diamond/SiC/CNT composites. In the meanwhile, we must note that the enhanced fracture toughness of our current composites compromises its hardness significantly. Compared to single crystal diamond, the measured fracture toughness was improved from 3-5 to 7-8 $MPa \cdot m^{1/2}$ while the hardness was reduced from 100 to 21 GPa. This inferior hardness may limit the practical use of composites in harsh environments of dynamic impacts and high stress concentrations.

IV.2. Diamond/CNT/SiC nanocomposites fabrication and characterization

In the previous chapter we investigated the reaction mechanism between Si and MWNTs under various conditions, and also we fabricated the CNT/SiC composites. Compared to diamond/SiC composites, the CNT/SiC composites do not possess clear superiority on mechanical features, particularly with aspect to hardness. In this section, we take advantage of the highest hardness feature of diamond to ameliorate the mechanical properties of composites, especially to improve hardness. This novel composite consists of diamond embedded into CNT/SiC matrix, which is anticipated to have both high hardness and enhanced fracture toughness. Four samples, C1 to C4 as listed in Table 4.2, were fabricated under 5 GPa and various temperatures. All these samples were made from a mixture of diamond powder of grain size 5-10 μm (General Electric Co.), Si with grain size of 30-70 nm, and MWNTs with the outer layer diameter from 10 to 30 nm in weigh ratio of 78:17:5. In order to mix the starting materials uniformly we applied ultrasonic mixing and mechanical rolling for 72 hours.

IV.2.1. X-ray diffraction patterns, crystallite size, and residual strain of the specimens

The XRD patterns for initial mixture and composites C1 and C4 are shown in the Fig. 4.5. Diamond peaks (111), (200), (220) were present in every pattern. The

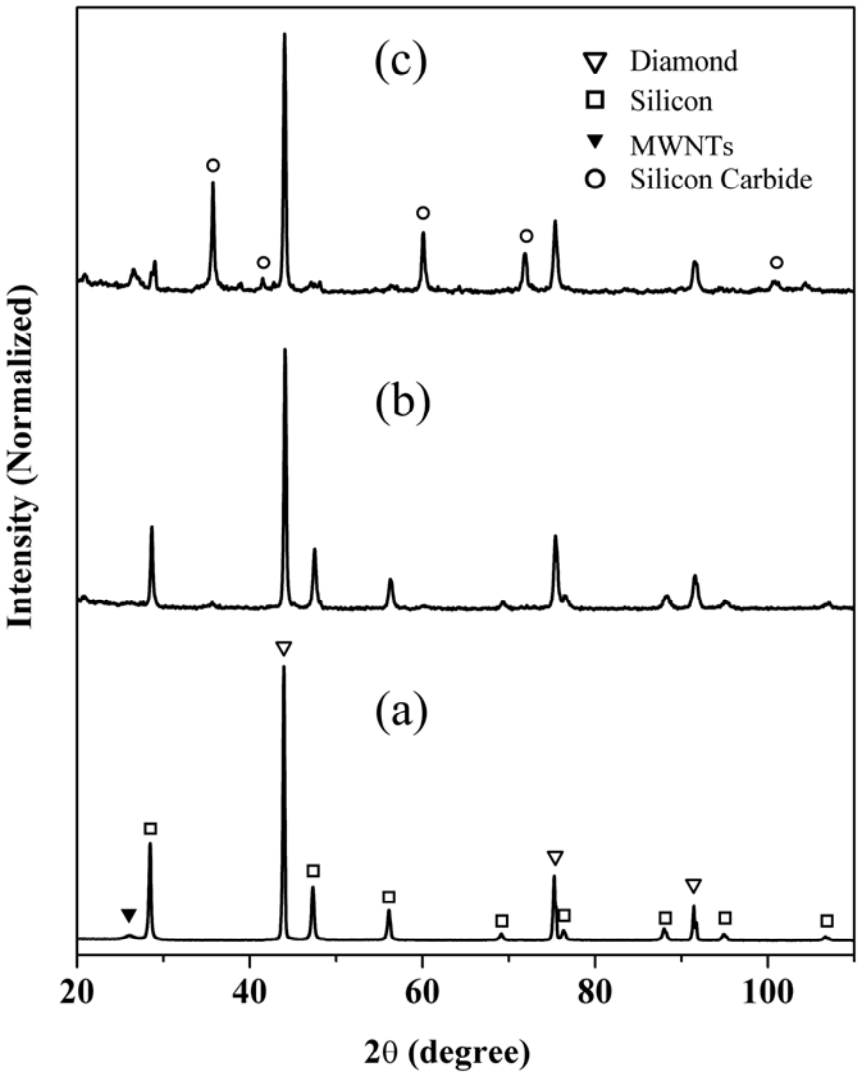

Fig. 4.5. X-ray diffraction patterns: (a) initial mixtures; (b) sample sintered under 5 GPa and 1570 K, C1: (c) sample sintered under 5 GPa and 2070 K, C4.

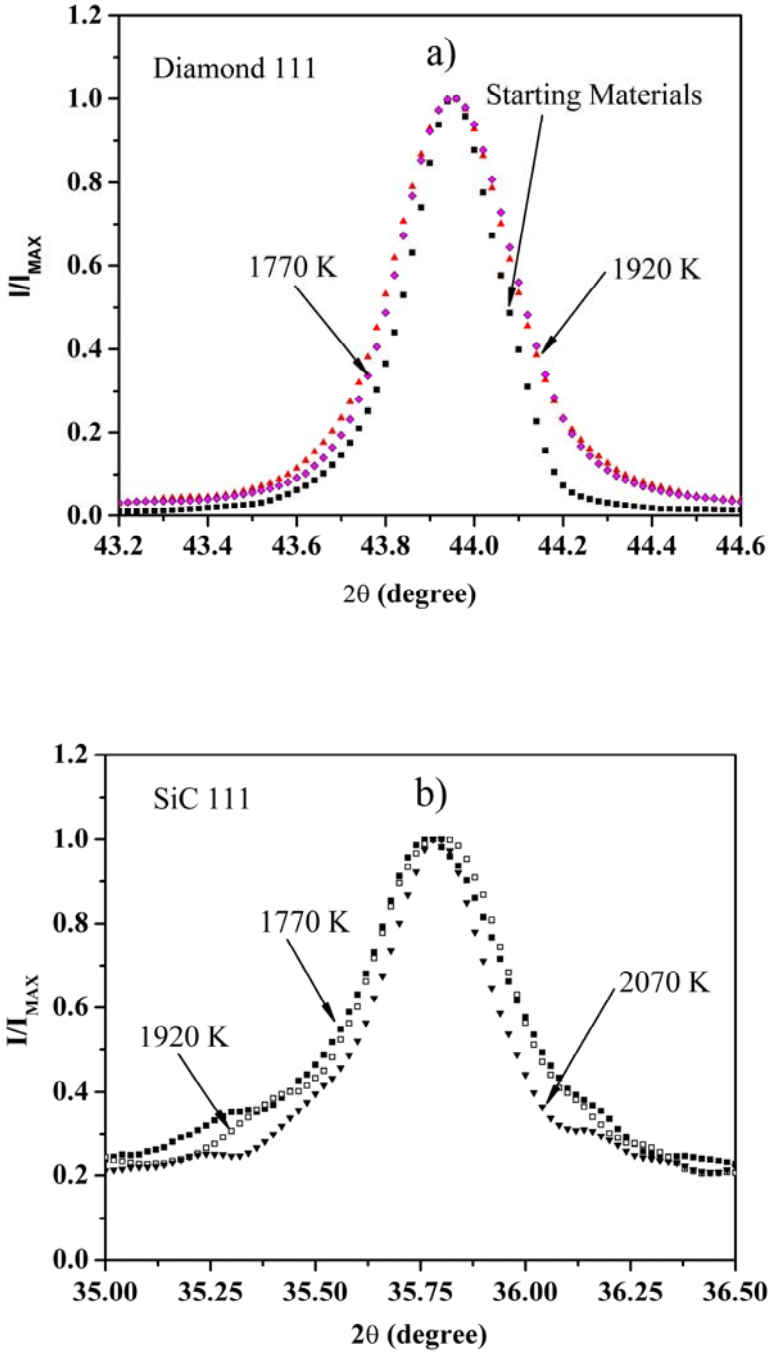

Fig. 4.6. The (111) line profiles for the diamond (a) and SiC (b) phases produced at different temperatures.

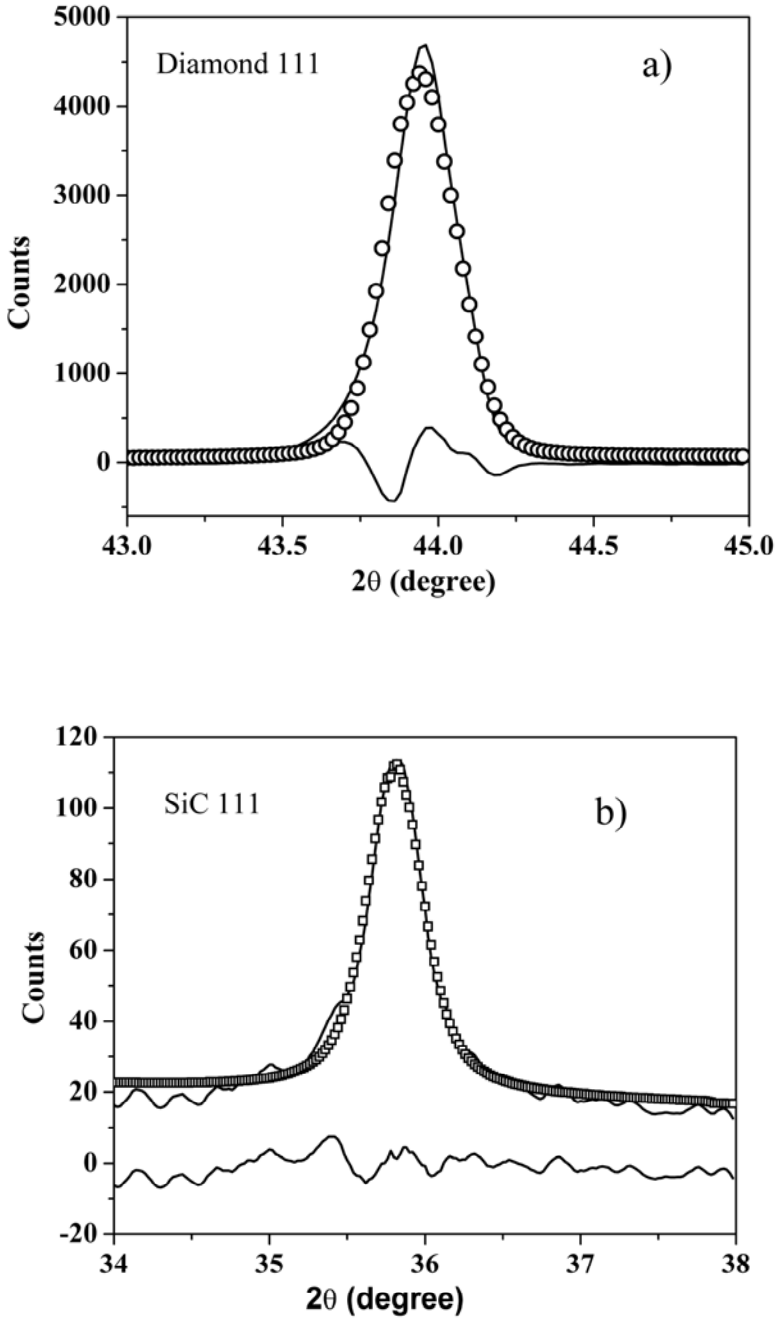

Fig. 4.7. Measured (solid line) and fitted (open circles) diffraction profiles of diamond (111) and SiC (111), and the difference between the two sets of curves is shown in the bottom part of the plot.

intensities of SiC peaks grow with increasing sintering temperature. There exists a very tiny peak near the SiC (111) reflection in C1 XRD patterns, however, for C4, the SiC peaks are evidently stronger. With the increasing temperature the Si peaks decrease and minute Si peaks are still located in the C4 pattern. Another worth noting phenomenon is that MWNTs are detected in all the patterns, and the intensities of MWNT peaks grow with increasing temperature. We did not observe any graphite or amorphous carbon from x-ray spectra.

The (111) peaks of diamond and SiC phases of composites show reverse trends. This can be observed in Fig. 4.6 where (111) reflections for the diamond and SiC phases are shown for initial diamond and produced at different temperatures. The diamond precursor has very small peak widths, and then with the temperature increasing, the diamond peaks broaden. For the SiC phase all peaks become narrower at high temperatures. We also noted unsymmetrical band shapes and smaller shoulders in the SiC diffractograms.

For domain sizes and microstrains of diamond and SiC, our investigation focused only on the (111) and (220) peaks. Other peaks were not taken into consideration due to their low intensities which may cause unexpected errors in calculations. The (111) and (220) peaks of diamond and SiC were refined by the double Voigt multiple-line integral-breadth method. As an example the fittings for the starting diamond and SiC phase of the composite formed at 1920 K are shown in Fig. 4.7. Using the (111) and (220) peaks as input profiles, the domain sizes and microstrains of diamond and SiC have been derived, and the results are depicted in Fig. 4.8 and Table 4.2.

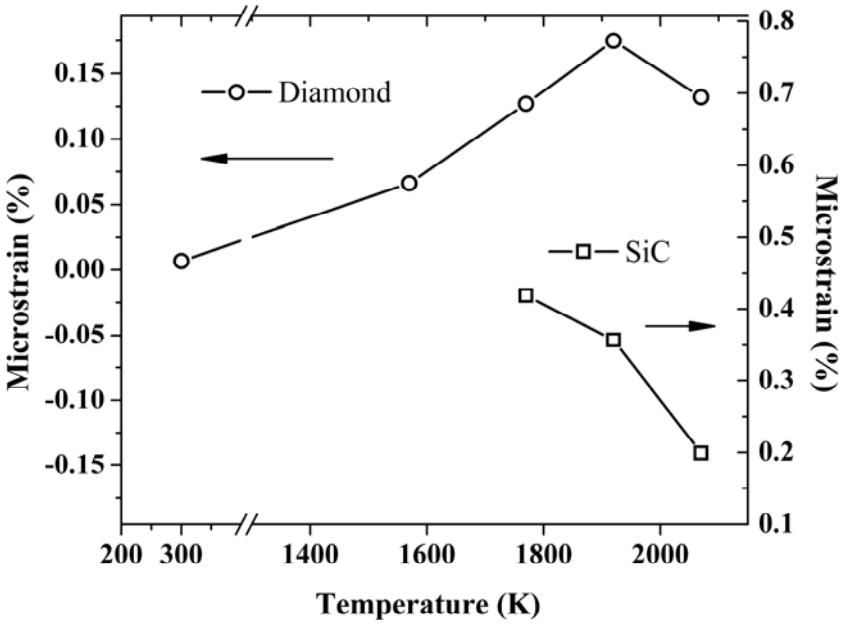

Fig. 4.8. Plot of microstrain in diamond and SiC vs. temperature.

The domain sizes of diamond decrease with increasing temperature, but they do not change significantly. However, for the SiC phase, the crystallites grow rapidly with temperature. For example, at the final temperature, the diamond domain size decrease by less than 20% compared to the starting materials. At the same time, the SiC domain size increases by more than 90%. The dislocation density of diamond increases continuously with increasing temperature up to 1920 K and then it abruptly drops. As expected, we observed the reduction of magnitude of remaining strain inside SiC phase. We also calculated the domain size and microstrain of initial diamond. The microstrain of initial diamond has been plotted in Fig. 4.8. Here we provide the domain size value of initial diamond, 369 (26) nm, which were not listed in Table 4.2. Because the amount of SiC

phase in sample C1 is too small to give an accurate result, we did not consider it in the microstructure analysis.

IV.2.2. SEM images and mechanical properties measurements

SEM photograph of sample C1 is shown in Fig. 4.9(a). Some large diamond grains approaching 5 μm can be clearly seen. It also shows high porosity of the sample. In addition to the presence of gaps and cavities we find SiC among diamond grains. In Fig. 4.9(b), the SEM images of sample C2, we can see a broad grain size distribution of diamond grains, ranging from sub micron to over 5 μm. Compare to Fig. 4.5(a), the average size of diamond grains appears to be smaller. It may be due to part of diamond conversion into SiC. Of course, we discover the tube-like structures, which may be formed from SiC coating CNT, fill the crevices between diamond grains.

For sample C3, its SEM photograph, shown in Fig. 4.9(c), manifests diamond tightly surrounded by SiC matrix. The size of diamond grains becomes more homogeneous compared to the first two samples.

Density, Vickers hardness, and fracture toughness were measured for all samples. We made five measurements on each sample, and then we took the average value as the final results. The hardness was almost constant on the whole surface. The indentations were examined by using SEM. Under loading force of 9.8 N, no cracks emerged at the corners of the indentation marks, shown in Fig. 4.10. The fracture toughness was examined with a larger loading force of 147 N. The densities of samples were measured by Archimedes method, and we used distilled water as the immersion medium. Data on

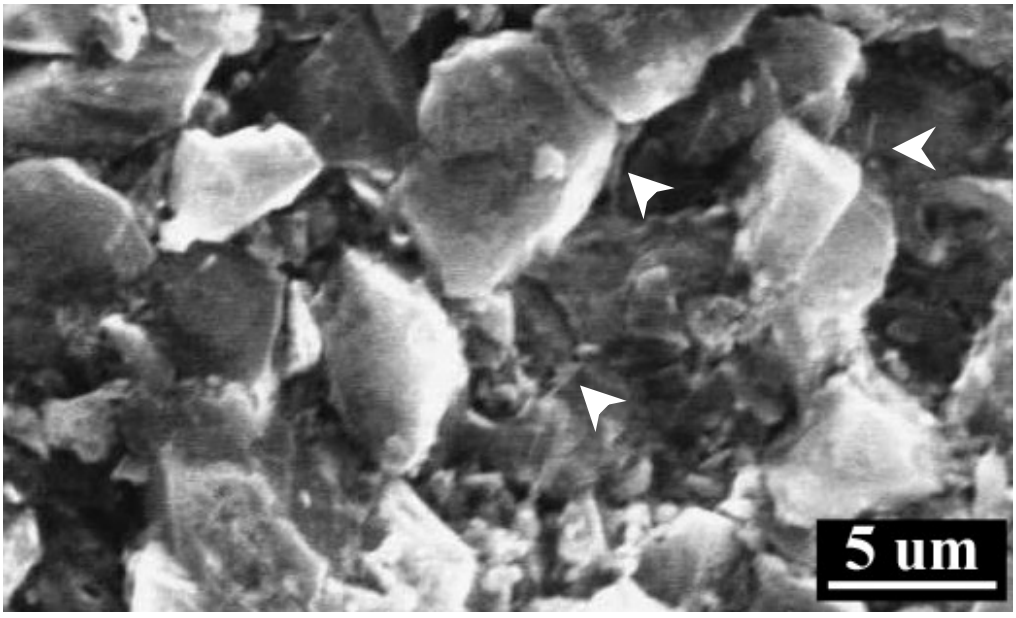

a)

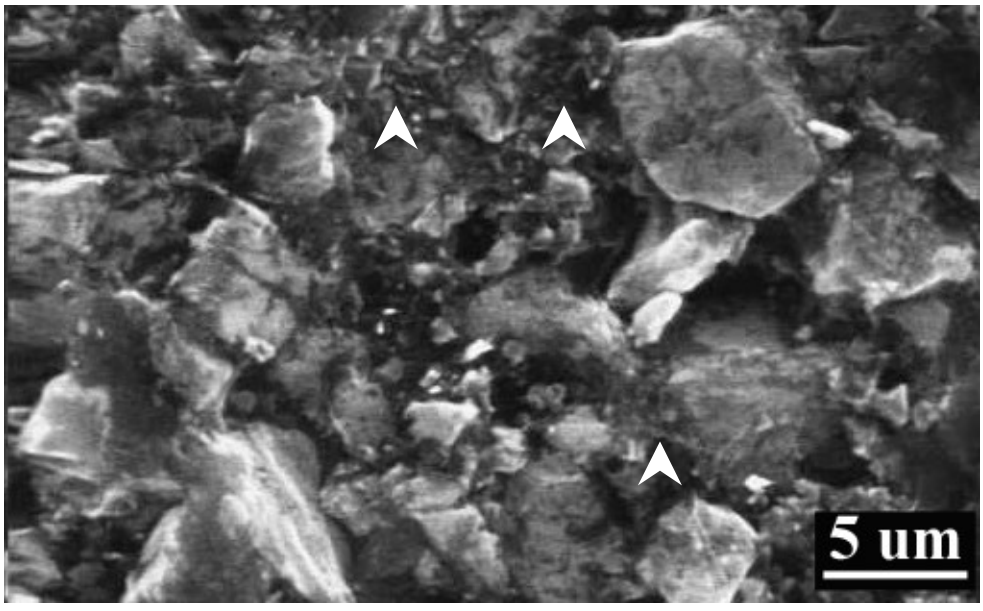

b)

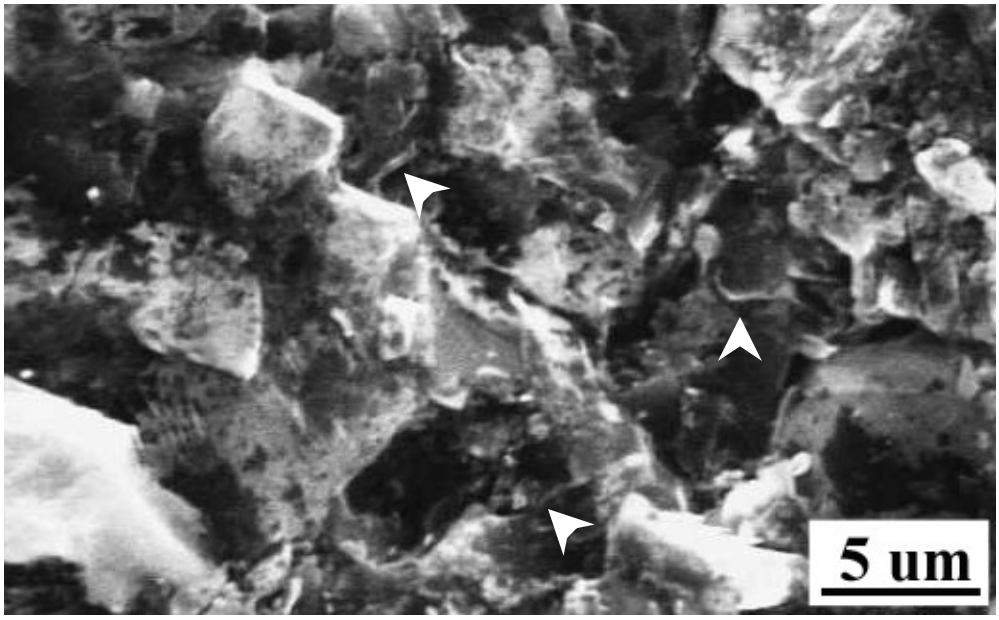

c)

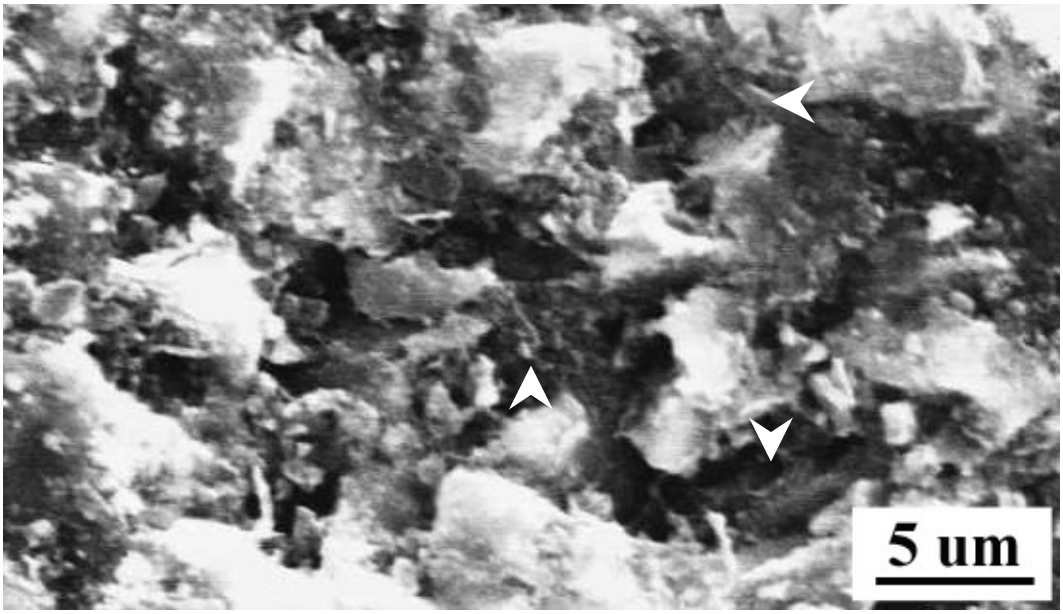

d)

Fig. 4.9. SEM images of composites, a) C1, b) C2, c) C3, d) C4. Arrows indicate tube-like structures present in the composites.

Table 4.2. Mechanical properties of composites. Uncertainty of the results is indicated by values in the parenthesis.

Sample	Sintering Temperature [K]	$\langle x \rangle_{vol}$ [nm]		Vickers Hardness H_V [GPa]	Fracture Toughness K_{IC} [MPa·m$^{0.5}$]
		Diamond	SiC		
C1	1570	269(24)	—	11(2)	—
C2	1770	332(24)	118(11)	24(1)	4.0(2)
C3	1920	314(48)	167(18)	33(5)	8.8(2)
C4	2070	299(32)	225(19)	32(3)	8.6(1)

hardness and fracture toughness are listed in Table 4.2. It reveals that all the measured data of mechanical properties increase with the temperature increment.

IV.2.3. Discussions

Since diamond crystals are broken into small size crystallites and additionally some carbon atoms react with silicon, it shows smaller sizes under HPHT compared to original diamond crystals. The plausible explanation is intense plastic deformation of diamond during heating at high pressure.[97] Of course few diamond grains sintered together and formed aggregated polycrystalline. For SiC growth, as expected, at higher temperature, atoms of carbon and Si possess more kinetic energy and participate in the reaction which leads to high SiC yield. These phenomena have been confirmed by XRD spectra and TEM images.

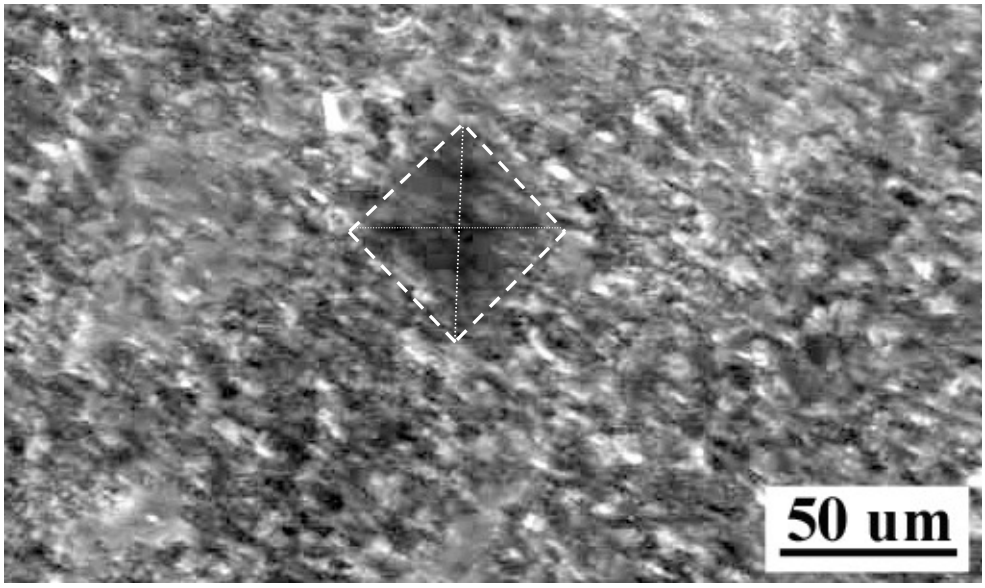

Fig. 4.10. SEM image of a Vickers indentation on composites C1.

Small shoulder on the low angle of (111) peak is due to stacking faults disorder during SiC formation under HTHP conditions. In the case of diamond, a large fraction of defects is expected to be concentrated at the contact points between two crystals, and the mobility of dislocation becomes intense with temperature increase.[97] At higher temperature, some dislocations may migrate into the interior of crystal, and new defects would grow near contacting surfaces of crystals. Consequently, the population of dislocation increases with temperature. At the highest temperature (2070 K), since the dislocation and vacancies in the surface layer of diamond are almost completely consumed by the carbon-silicon reaction, as indicated in Fig. 4. 9 (d), the dislocations in diamond are annihilated. For diamond and SiC produced at 2070 K, the smaller peak

width originate from the larger grain size and lower dislocation density, but here we can not define which effect contributes more to this phenomenon.

Larger value of density of specimens indicates that at higher temperature silicon fills more pores or voids between diamond crystals to form denser composites. More importantly, mechanical properties of composites increase with density, such as hardness and fracture toughness. It may exist a relationship between the extent of bonding of carbon nanotubes in the matrix and the density of composites. In consolidated composites, the MWNTs and SiC are inseparably entangled with diamond crystals. As mentioned earlier, the MWNTs are distributed along the grain boundary of diamond to form a network structure. The intimate contacts among MWNTs, diamond, and SiC make it possible to transfer load to carbon nanotubes and the carbon nanotubes prevent the cracks from further propagation. Most likely, cracks occur at defective points of the composites. To grow further, the crack would have to break through the carbon nanotubes network. Also due to the superior elasticity of carbon nanotube inserted in composites, it could work as a damping to absorb the vibration energy and cut down the intensity of shock waves externally applied to the composites. The high Young's modulus of carbon nanotubes together with the mobility reduction of cracks results in an improvement of fracture toughness of composites.

Compared to the MWNT/SiC composites, studied in the previous section, both hardness and fracture toughness of diamond/SiC/MWNTs have improved. For example, the measured fracture toughness of the present composites is at the similar level to that of the MWNTs/SiC composites described in the previous section, while the measured

hardness is enhanced as much as 50%. The involvement of diamond in composites manufacture is beneficial to the hardness improvement.

In summary, our study demonstrates that carbon nanotubes are a promising candidate to toughen the ceramic materials. It is probably possible to produce even higher quality composites by homogeneously dispersing carbon nanotubes in the SiC matrix and minimizing the porosity in the samples.

V. Summary and future work

Even after long-term efforts made by scientific and industrial communities, there still exist some problems impeding the diamond composites application. Among them, the most critical drawback is their brittleness, which not only shortens their lifetime when used in harsh environment but also raises the cost of production. For example, in oil drilling field, increasing the lifetime of rock cutting inserts by 23 to 26 % can save $ 77,000 per well in an average. Hence improvements of their mechanical properties or invention of other replaceable material with better fracture toughness are desperately needed. Performance of materials depends on their properties. We may enhance their properties by tailoring the corresponding atomic structure, composition, microstructure, defects, and interfaces between multiple phases. As mentioned before, our group collaborated with another lab and has successfully synthesized nanostructured diamond-SiC composites from high-energy ball-milled precursor mixtures. The HTHP fabricated products are well-sintered, highly dense nanostructured bulks with enhanced yield strength and high toughness to fracture.

In this dissertation we explored the possibility to reinforce the diamond composites by applying carbon nanotubes or SiC nanowires. This is an extension of the above research scope. It covered three perspectives. First, we tried to fabricate SiC nanowires and build a relationship between the morphology of products and the reaction conditions. Secondly, we studied the kinetics of SiC formation from Si and CNT, and we also discovered that CNT needed relatively low energy injected externally to form SiC compared to other carbon phases, like graphite and diamond. Finally we synthesized CNT/SiC and diamond/CNT/SiC composites.

Although many methods of producing SiC nanowires/nanorods exist, here we developed new approach to synthesize two distinctly different kinds of SiC nanowires by simply heating the mixture of Si and CNT. Our study showed that the final products greatly depended on the heating temperature. We carried out experiments in the solid and liquid regions of Si. SiC nanowires grown via the solid-state reaction had similar diameters and smooth surfaces, with of course some SiC grains intermingled. Even though the reaction mechanism is still not completely understood, with the assistance of TEM images, we may say that some silicon and carbon atoms on the surface of CNT possess enough kinetic energy to participate in the reaction, but the reason why SiC grows into wires instead of other shapes is still not understood clearly. At higher temperature under which Si liquefies, the products were in the form of tube structures with coarse, flake-like structures mounted on the surface of CNT, and their diameters were bigger than those of initial CNT. The XRD patterns and Raman spectra proved that the composition of these novel structures was not only pure SiC, but also included carbon. By careful analysis of TEM images we found that the new grown materials were not solid rods but tube-like structures. It is reasonable to hypothesize that the carbon atoms in the outer layers of CNT reacted with liquid Si and transformed into SiC while the inner core of CNT was left intact. Simply speaking, these unique coaxial structures were formed by SiC coating CNT. In the current situation CNT provided carbon source, and simultaneously CNT worked as a template to constrain and determine the shape morphology of the final products. When we applied external pressure during high temperature heating, some carbon nanotubes became straight SiC rods. Unfortunately, population of solid rods was low and SiC existed mainly in the form of irregular particles.

Following the SiC nanowires synthesis, we performed the kinetics study of SiC formation from CNT and nanocrystalline Si. Based on the Avrami-Erofeev model we found the activation energy of silicon carbide to be 96.1 ± 28.7 kJ/mol. Our results demonstrate that CNT may have higher chemical reactivity than other forms of elemental carbon, which could be ascribed to high population of defects on CNT surface. Analysis of x-ray diffraction patterns provided information on domain sizes and microstrain in SiC. Longer sintering time increased grain sizes and decreased microstrain in SiC, and increased temperature resulted in larger crystallites.

Finally we tried to make CNT based superhard composites. Two series of samples we made: CNT/SiC and CNT/diamond/SiC. For CNT/SiC composites fabrication, experiments were carried out at 2 GPa and 8 GPa, and 1770 and 1970 K. XRD and Raman confirmed that CNT could maintain their unique structures during reaction with Si under HTHP conditions and could be used as a reinforcement phase to improve toughness of composites. However, the relatively low hardness decreases their practical application. Production of CNT/diamond/SiC composites appears to be more promising. These composites have pronounced nanocrystalline structure and interesting mechanical properties. For example, the measured fracture toughness was similar to that of CNT/SiC composites, while the hardness improved as much as 50 %. However, in comparison with the best results obtained for diamond/SiC nanocomposites, mechanical properties of current diamond/SiC/CNT did not show significant advantages. Additional studies are necessary to explore potential of CNT in improving mechanical properties of composites. One option is to disperse nanotubes more homogeneously in the initial mixture. Previously, we used ultrasonic processor and roller mixer to mix the starting

materials. In the future we may try a ball-milling method to transform Si into amorphous phase and improve contacts between Si and CNT.

We also would like to use *in-situ* time-of-flight neutron (LANSCE) and synchrotron x-ray (NSLS) diffractions at simultaneous high pressures and high temperatures to monitor the sintering process in *real-time* and map out the phase diagrams in *P-T-X* space. Time-resolved measurements could be carried out to characterize grain growth, stress relaxation, and plastic deformation at high *P-T* conditions. Comparative studies on selected samples could be carry out to illustrate the property alternations as the grain size change from micron- to nano- scale and from amorphous to crystalline forms. We could also carry out TEM work associated with indentation and bending studies to understand the novel behaviors of nanocomposites and amorphous boundaries in terms of crack initiation and propagation mechanisms. Our *in-situ* and *real-time* diagnostic technique could help greatly in optimizing the sintering process and in improving the quality of bulk nanostructured products. The recovered samples could be characterized in terms of mechanical, magnetic, electric, and electronic properties to explore their functional capabilities and possible industrial applications.

References:

1) J. P. Schaffer, A. Saxena, T. H. Senders, S. D. Antolovich, and S. B. Warner, *The science and design of engineering materials*, published by IRWIN [now McGraw-Hill], Chicago

2) http://www.composites-by-design.com/metal-matrix.htm

3) J. Qian, T. W. Zerda, D. He, L. Daemen, and Y. Zhao, *J. Mar. Res.* 18, 1173 (2003)

4) J. Qian, G. Voronin, T. W. Zerda, D. He, and Y. Zhao, *J. Mar. Res.* 17, 2153 (2002)

5) G. A. Voronin, T. W. Zerda, J. Qian, Y. Zhao, D. He, and S. N. Dub, *Diam. Relat. Mater.* 12, 1477 (2003)

6) G. A. Voronin, T. W. Zerda, J. Gubicza, T. Ungar, and S. N. Dub, *J. Mar. Res.* 19, 2703 (2004)

7) Y. Zhao, J. Qian, L. L. Daemen, C. Pantea, J. Zhang, G. A. Voronin, and T. W. Zerda, *Appl. Phys. Lett.* 84, 1356 (2004)

8) J. Gubicza, T. Ungár, Y. Wang, G. Voronin, C. Pantea, and T. W. Zerda, *Diam. Relat. Mater.* in press (2006)

9) J. Qian, *Diamond/Silicon Carbide Composites Sintering under High Pressure-High Temperature Conditions* (Doctoral Thesis, Texas Christian University, Fort Worth, TX 2003)

10) G. A. Voronin, S. A. Osipov, and A. A. Shulzhenko, *Miner. J.* 17, 90 (1995)

11) G. A. Voronin, *Proceedings of Joint AIRAPT-16 & HPCJ-38 Int. Conf.*, Jap. Soc. High Pressure Sci. Technol. Kyoto, Japan, 467 (1997)

12) O. S. Osipov, A. L. D. Skury, and G. S. Bobrovnitchii, *Mater. Res.* 7, 335 (2004)

13) H. Sumiya and S. Satoh, *J. Refract. Met. & Hard Mater.* 17, 345 (1999)

14) I. E. Clark and P. A. Bex, *Indust. Diamond Rev.* 1, 43 (1999)

15) P. N. Tomlism, N. J. Pipkin, A. Lammer, and R. P. Burnand, *Indust. Diamond Rev.* 6, 299 (1985)

16) W. Tillmann, *J. Refract. Met. & Hard Mater.* 18, 301 (2000)

17) O. Osamu, O. Naoyuki, K. Katsuyuki, A. Hiroshi, F. Hiroshi, Y. Takamitsu, M. Kei, I. Suguru, K. Takumi, and S. Masaru, *J. High Press. Res.* 25, 11 (2005)

18) R. Riedel, *Handbook of Ceramic Hard Materials* (Wiley-VCH, Weinheim, 2000)

19) P. A. Bex and G. R. Shafto, *Ultrahard Mater. Appl. Technol.* 3, 22 (1984)

20) E. A. Ekimov, A. G. Gavriliuk, B. Palosz, S. Gierlotka, P. Dluzewski, E. Tatianin, Yu. Kluev, A. M. Naletov, and A. Presz, *Appl. Phys. Lett.* 77, 954 (2000)

21) C. Pantea, G. A. Voronin, T. W. Zerda, J. Zhang, L. Wang, Y. Wang, T. Uchida, and Y. Zhao, *Diam. Relat. Mater.* 14, 1611 (2005)

22) C. Pantea, G. A. Voronin, and T. W. Zerda, *J. Appl. Phys.* 98, 073512 (2005)

23) http://newton.ex.ac.uk/research/qsystems/people/sque/diamond/

24) F. P. Bundy, *J. Chem. Phys.* 38, 631 (1963)

25) H. T. Hall, *Science*, 169, 868 (1970)

26) R. H. Wentorf, R. C. Devries, and F. P. Bundy, *Science*, 208, 873 (1980)

27) F. P. Bundy and W. A. Bassett, *Carbon*, 34, 141 (1996)

28) H. T. Hall, *Polycrystalline Diamond Composites:* U. S. Patent No. 3, 913, 280 (1975)

29) K. Kurihara, K. Sasaki, M. Kawarada, and N. Koshino, *Appl. Phys. Lett.* 52, 437 (1988)

30) G. W. Robert and F. Davis, *Proc. of the Inter. Conf. in SiC and Relat. Mater. -93*, Washton DC, USA, November 1-3, 1993, *Inst. Phys. Conf. Ser*. 137, 1 (1994)

31) J. J. Berzelius, *Ann. Phys*. Lpz. 1, 169 (1824)

32) A. H. Cowles and E. H. Cowles, *U. S. Pat.* 319945 (1885)

33) A. G. Acheson, *Engl. Pat.* 17911(1892)

34) G. Meng, L. Zhang, C. Mo, S. Zhang, Y. Qin, S. Feng, and H. Li, *J. Mater. Res.* 13, 2533 (1998)

35) B. Palosz, E. Grzanka, S. Gierlotka, S. Stelmakh, R. Pielaszek, W. lojkowski, U. Bismayer, J. Neuefeind, H. Weber, and W. Palosz, *Phase Transit.* 76, 171 (2003)

36) E. W. Wong, P. E. Sheehan, and C. M. Lieber, *Science*, 266, 1971 (1997)

37) H. Dai, E. W. Wong, Y. Lu, S. Fan, and C. M. Liber, *Nature*, 375, 769 (1995)

38) W. Han, S. Fan, Q. Li, W. Liang, B. Gu, and D. Yu, *Chem. Phys. Lett.* 265, 374 (1997)

39) Y. Gao, Y. Bando, K. Kurashima, and T. Sato, *Scripta mater.* 44, 1941 (2001)

40) X. Zhou, N. Wang, H. Lai, H. Peng, I. Bello, N. B. Wong, C. S. Lee, and S. T. Lee, *Appl. Phys. Lett.* 74, 3942 (1999)

41) H. Lai, N. Wong, X. Zhou, H. Peng, F. C. K. Au, N. Wang, I. Bello, C. S. Lee, S. T .Lee, and X. Duan, *Appl. Phys. Lett.* 76, 294 (2000)

42) Q. Lu, J. Hu, K. Tang, Y. Qian, G. Zhou, X. Liu, and J. Zhu, *Appl. Phys. Lett.* 75, 507 (1999)

43) J. Liu, D. Zhong, F. Xie, M. Sun, E. Wang, and W. Liu, *Chem. Phys. Lett.* 348, 357 (2001)

44) H. W. Kroto, J. R. Heath, S. C. O'brien, R. F. Curl, and R.E. Smalley, *Nature*, 318, 162 (1985)

45) http://www.nanotech-now.com/nanotube-buckyball-sites.htm

46) S. Iijima, *Nature*, 354, 56 (1991)

47) S. Iijima and T. Ichihashi, *Nature*, 363, 603 (1993)

48) E. D. Minot, Y. Yaish, V. Sazonova, J. Park, M. Brink, and P. L. McEuen, *Phys. Rev. Lett.* 90, 156401 (2003)

49) B. I. Yakobson, C. J. Brabec, and J. Bernholc, *Phys. Rev. Lett.* 76, 2511 (1996)

50) M. Yu, B. S. Files, S. Arepalli, and R. S. Ruoff, *Phys. Rev. Lett.* 84, 5552 (2000)

51) R. Z. Ma, J. Wu, B. Q. Wei, J. Liang, and D. H. Wu, *J. Mater. Sci.* 33, 5243 (1998)

52) D. Qian, E. C. Dickey, R. Andrews, and T. Rantell, *Appl. Phys. Lett.* 76, 2868 (2000)

53) P. McNutt, *Piston-cylinder manual*, Rockland Research Corp (1996)

54) C. Pantea, *Diamond – Silicon Reaction under High Pressure-High Temperature Condition* (Doctoral Thesis, Texas Christian University, Fort Worth, TX 2004)

55) J. I. Langford and D. Louer, *Powder diffraction*, *Rep. Prog. Phys.* 59, 131 (1996)

56) H. P. Klug and L. E. Alexander, *X-ray Diffraction Procedures For Polycrystalline and Amorphous Materials*, John Wiley & Sons (1974)

57) D. Balzar, *Voigt-Function Model in Diffraction Line-Broadening Analysis*, in *Defect and Microstructure Analysis from Diffraction*, edited by R.L. Snyder, H.J.

Bunge, and J. Fiala, International Union of Crystallography Monographs on Crystallography No. 10 (Oxford University Press, New York, 1999) pp. 94

58) B. E. Warren and B. L. Averbach, *J. Appl. Phys.* 21, 595 (1950)

59) B. E. Warren, *Prog. Met. Phys.* 8, 147 (1959)

60) H. M. Rietveld, *Acta Crystallogr*. 22, 151 (1967)

61) S. A. Howard and R. L. Snyder, *J. Appl. Cryst.* 22, 238 (1989)

62) J. K. Yau and S. A. Howard, *J. Appl. Cryst.* 22, 244 (1989)

63) D. Balzar, *J. Appl. Cryst.* 28, 244 (1995)

64) D. Balzar and H. Ledbetter, *J. Appl. Cryst.* 26, 97 (1993)

65) D. Balzar, *J. Res. Natl. Inst. Stand. Technol.* 98, 321 (1993)

66) W. Demtroder, *Laser Spectroscopy,* Springer

67) http://www.chem.ucl.ac.uk/resources/raman/speclib.html

68) D. H. Rank and J. S. McCartney, *J. Opt. Soc. Am.* 38, 279 (1948)

69) G. Placzek, *Rayleigh-Streuung and Raman Effekt*, in handbuch der Radiologie. Vol. VI, edited By E. Marx (Akademische Verlagsgesellschaft, Leipzig 1934)

70) H. S. Ray, *Kinetics of Metallurgical Reactions,* Oxford & IBH Publishing Co. PVT. LTD (1993)

71) M. Avrami, *J. Chem. Phys.* 7, 1103 (1939)

72) B. V.Erofeev, *Compt. Rend. Acad. Sci.* USSR 52, 511 (1946)

73) Z. C. Feng, A. J. Mascarenhas, W. J. Choyke, and J. A. Powell, *J. Appl. Phys.* 64, 3176 (1998)

74) K. Huang, B. E. Zhu, and H. Tang, *Phys. Rev. B: Solid State* 41, 5825 (1990)

75) D. Olego and M. Cardona, *Phys. Rev. B* 25, 1151 (1982)

76) D. Olego and M. Cardona, *Phys. Rev. B* 25, 3878 (1982)

77) E. Yu. Tonkov, *High Pressure Phase Transformations,* Gordon and Breach Science Publishers

78) W. A. de Heer and D. Ugarte, *Chem. Phys. Lett.* 207, 480 (1993)

79) M. Mouthioux and G. J. Lavin, *Carbon*, 335, 32 (1994)

80) P. Zhang, P. E. Lammert, and V. H. Crespi, *Phys. Rev. Lett.* 81, 5346 (1998)

81) A. Hashimoto, K. Suenaga, A. Gloter, K. Urita, and S. Iijima, *Nature*, 430, 870 (2004)

82) N. Chakrapani, Y. M. Zhang, S. K. Nayak, J. A. Moore, D. L. Carroll, Y. Y. Choi, and P. M. Ajayan, *J. Phys. Chem. B* 107, 9308 (2003)

83) S. Picozzi, S. Santucci, L. Lozzi, L. Valentini, and B. Delley, *J. Chem. Phys.* 120, 7147 (2004)

84) B. Palosz, E. Grzanka, S. Stel'makh, S. Gierlotka, R. Pielaszek, U. Bismayer, H. P. Weber, T. H. Proffen, and W. Palosz, *Solid State Phenom*. 94**,** 203 (2003)

85) V. I. Gorovenko, V. A. Knyazik, and A. S. Shteinberg, *Ceram. Int.* 19, 129 (1993)

86) C. Pantea, G. A. Voronin, T.W. Zerda, J. Zhang, L. Wang, Y. Wang, T. Uchida, and Y. Zhao, *Diam. Relat. Mater.* 14, 1611 (2005)

87) N. Chakrapani, Y. M. Zhang, S. K. Nayak, J. A. Moore, D. L. Carroll, Y. Y. Choi, and P. M. Ajayan, *J. Phys. Chem. B* 107, 9308 (2003)

88) G. W. Ho, A. S. W. Wong, A. T. S. Wee, and M. E. Welland, *Nano Lett.* 4, 2023 (2004)

89) S. Zhang, B. Zhu, F. Huang, Y. Yan, E. Shang, S. Fan, and W. Han, *Solid State Commun.* 111, 647 (1999)

90) M. Wieligor, Y. Wang, and T. W. Zerda, *J. Phys.: Condens. Matter*,17, 2387 (2005)

91) E. Muñoz, A. B. Dalton, S. Collins, A. A. Zakhidov, R. H. Baughman, W. L. Zhou, J. He, C. J. O'Connor, B. McCarthy, and W. J. Blau, *Chem. Phys. Lett.* 359, 397 (2002)

92) G. A. Voronin, T. W. Zerda, J. Qian, Y. Zhao, D. He, and S. N. Dub, *Diamond Relat. Mater.* 12, 1477 (2003)

93) S. Rohmfeld, M. Haundhausen, and L. Ley, *Phys. Rev. B* 58, 9858 (1998)

94) J. F. DiGregorio, T. E. Furtak, and J. J. Petrovic, *J. Appl. Phys.* 71, 3524 (1992)

95) G. Zhan, J. D. Kuntz, J. Wan, and A. K. Mukherjee, *Nat. Mater.* 2, 38 (2003)

96) S. Seal, S. C. Kuiry, P. Georgieva, and A. Agarval, *MRS Bull.* 29, 16 (2004)

97) C. Pantea, J. Gubicza, T. Ungár, G. Voronin, and T. W. Zerda, *Phys. Rev. B* 66, 094106 (2002)

Symbols

2θ	the fixed scattering angle
α	degree of reaction
α	lattice constant
α	polarizability
α_0	polarizability at the equilibrium position
a	lattice constant (Å)
A	pre-exponential factor in the Arrhenius equation
β	lattice constant
β_C	Cauchy integral breadths of the Voigt function
β_{DC}	the distortion component of Cauchy integral breadths of the Voigt function
β_{DG}	the distortion component of distortion integral breadths of the Voigt function
β_G	Gauss integral breadths of the Voigt function
β_{SC}	the size component of Cauchy integral breadths of the Voigt function
β_{SG}	the size component of Gauss integral breadths of the Voigt function
b	lattice constant (Å)
B	The full width at half maximum
c	lattice constant (Å)
C	Vickers indentation crack length
d	lattice interplanar distance
D	Vickers indentation diagonal length
$< D >_s$	surface-weighted domain size (nm)

$< D >_v$ volume-weighted domain size (nm)

Δl path difference

E electric field

E Young's modulus (GPa)

E_a activation energy (kJ/mol)

ε Upper limit of strain from the simplified integral-breadth methods

f Pure-specimen (physically) broadened profile

F loading force (N)

g Instrumentally broadened profile

γ lattice constant

γ chiral angle of carbon nanotubes

h Observed broadened profile

H_K Knoop hardness (GPa)

H_V Vickers hardness (GPa)

hkl Miller indices

$I_{\max}$ the maximum intensity of single peak of x-ray diffraction

k reaction rate constant (s^{-1})

k the characteristic integral-breadth ratio of a Voigt function

K the Scherrer constant

K_{IC} fracture toughness

λ wavelength (nm)

m a kinetics parameter describing the growth type of a reaction

$m_{SiC}^{as-grown}$ mass of SiC produced

$m_{Si}^{initial}$ mass of Si before reaction

$m_{Si}^{reacted}$ mass of Si consumed during reaction

$m_{Si}^{remaining}$ mass of unreacted Si

v_o frequency of incident phonon

v_m frequency of crystal molecule

P polarization

P mass of object in air

p mass of object in water

q nuclear displacement

q_0 vibrational amplitude of molecule

R gas constant

s $2\sin\theta/\lambda=1/d$, variable in reciprocal space.

s_o $2\sin\theta/\lambda=1/d$, variable in reciprocal space taken for the first peak

S specific gravity

t time

t thickness of crystal

T temperature

θ_B Bragg angle

R reaction rate

$< X >_{vol}$ volume-weighted domain size (nm)

VITA

Personal Background

Yuejian Wang
Born November 10, 1971, Yuanping, Shanxi Province, P. R. China
Son of Gaoke Wang and Guimei Zhao
Married Xinxin Liu on July 14, 2004
One child

Education

Diploma, Fanting High School, Yuanping, Shanxi Province, P. R. China, 1990
Bachelor of Engineering, Mechanical Engineering, Taiyuan University of Technology, Taiyuan, P. R. China, 1994
Bachelor of Engineering, Engineering Physics, Tsinghua University, Beijing, P. R. China, 1996
Master of Science, Physics, Stephen F. Austin State University, Nacogdoches, Texas, 2002
Doctor of Philosophy, Physics, Texas Christian University, Fort Worth, 2006

Experience

Engineer, Nuclear Fuel Enrichment at The 7th Research and Design Institute, Taiyuan City, China National Nuclear Corporation (CNNC), P. R. China, 1996 – 2000
Engineer, Technology Support at Daya Bay Nuclear Power Station, Shenzhen, P. R. China, 1998
Teaching Assistant, Stephen F. Austin State University, Nacogdoches, Texas, 2000 – 2002
LANSCE Neutron Scattering Winter School at Los Alamos National Laboratory, Los Alamos, NM, 2005
Carnegie/DOE Alliance Center (CDAC) Summer School on High Pressure-Temperature Materials Research at Advanced Photon Source, Argonne National Laboratory, Argonne, IL, 2005
Research/Teaching Assistantship, Texas Christian University, Fort Worth, TX, 2002 – 2006
Graduate Research Assistantship, Los Alamos National Laboratory, 2006 – Present

ABSTRACT

SILICON CARBIDE NANOWIRES AND COMPOSITES
OBTAINED FROM CARBON NANOTUBES

By Yuejian Wang, Ph. D., 2006
Department of Physics & Astronomy
Texas Christian University

T. W. Zerda, Professor and Chair of Physics of Physics & Astronomy
W. R. M. Graham, Professor of Physics & Astronomy
C. A. Quarles, Professor of Physics & Astronomy
Y. M. Strzhemechny, Professor of Physics & Astronomy

In this dissertation a simple route has been developed to synthesize Silicon Carbide (β-SiC) nanothreads and C-SiC coaxial nanotubes by solid/liquid-state reaction between multiwall carbon nanotubes and silicon conducted at 1473 K and 1723 K, respectively. Through the kinetics study of SiC formation from carbon nanotubes and Si, our results demonstrated that carbon nanotubes may have higher chemical reactivity than other forms of elemental Carbon. Based on the above investigation, CNT/SiC and diamond/CNT/SiC were manufactured. Key factors influencing the mechanical properties of final products, such as phase composition, grain size, stress-strain, sintering time, and sintering temperature were thoroughly studied with Raman spectroscopy, x-ray diffraction, SEM and TEM techniques. Taking advantage of high elasticity of Carbon nanotube and its ability to block the microcrack propagation and dislocation movement, both composites showed enhanced fracture toughness. Carbon nanotubes composites trigger a new field in fundamental science and manifest potential application in multiple industries.